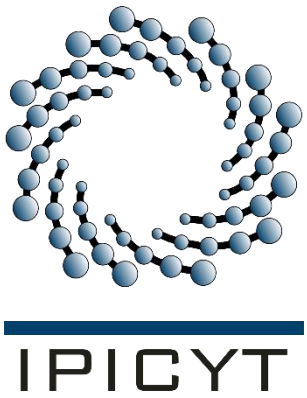

INSTITUTO POTOSINO DE INVESTIGACIÓN CIENTÍFICA Y TECNOLÓGICA, A.C.

POSGRADO EN NANOCIENCIAS Y MATERIALES

Highly efficient production of nitrogen-doped multiwalled carbon nanotubes using banded iron formation from the Bundelkhand craton located in the north of India.

Tesis que presenta
Luis Ernesto Jiménez Ramírez

Para obtener el grado de
Maestro en Nanociencias y Materiales

Director de la Tesis

Florentino López Urías

San Luis Potosí, S.L.P., a 20 agosto 2018

Constancia de aprobación de la tesis

La tesis "**Highly efficient production of nitrogen-doped multiwalled carbon nanotubes using banded iron formation from the Bundelkhand craton located in the north of India**" presentada para obtener el Grado de Maestro en Nanociencias y Materiales fue elaborada por **Luis Ernesto Jiménez Ramírez** y aprobada el **20 de Agosto de 2018** por los suscritos, designados por el Colegio de Profesores de la División de Materiales Avanzados del Instituto Potosino de Investigación Científica y Tecnológica, A.C.

_____

Dr. Florentino López Urías
Director/Codirectores de la tesis

_____

Dr. Armando Encinas Oropesa
Miembro del Comité Tutoral

_____

Dr. Emilio Muñoz Sandoval
Miembro del Comité Tutoral

Créditos Institucionales

Esta tesis fue elaborada en las instalaciones y con infraestructura de la División de Materiales Avanzados del Instituto Potosino de Investigación Científica y Tecnológica, A.C. y el Laboratorio de Investigaciones en Nanociencia y Nanotecnología, bajo la dirección del doctor Florentino López Urías.

Durante la realización del presente trabajo el autor recibió una beca académica del Consejo Nacional de Ciencia y Tecnología en México (605694)

IPICYT

Instituto Potosino de Investigación Científica y Tecnológica, A.C.

Acta de Examen de Grado

El Secretario Académico del Instituto Potosino de Investigación Científica y Tecnológica, A.C., certifica que en el Acta 041 del Libro Primero de Actas de Exámenes de Grado del Programa de Maestría en Nanociencias y Materiales está asentado lo siguiente:

En la ciudad de San Luis Potosí a los 24 días del mes de agosto del año 2018, se reunió a las 16:00 horas en las instalaciones del Instituto Potosino de Investigación Científica y Tecnológica, A.C., el Jurado integrado por:

Dr. Armando Encinas Oropesa	**Presidente**	**IPICYT**
Dr. Jesús Iván Tapia López	**Secretario**	**IPICYT**
Dr. Florentino López Urías	**Sinodal**	**IPICYT**

a fin de efectuar el examen, que para obtener el Grado de:

MAESTRO EN NANOCIENCIAS Y MATERIALES

sustentó el C.

Luis Ernesto Jiménez Ramírez

sobre la Tesis intitulada:

Highly efficient production of nitrogen-doped multiwalled carbon nanotubes using banded iron formation from the Bundelkhand craton located in the north of India

que se desarrolló bajo la dirección de

Dr. Florentino López Urías

El Jurado, después de deliberar, determinó

APROBARLO

Dándose por terminado el acto a las 16:50 horas, procediendo a la firma del Acta los integrantes del Jurado. Dando fe el Secretario Académico del Instituto.

A petición del interesado y para los fines que al mismo convengan, se extiende el presente documento en la ciudad de San Luis Potosí, S.L.P., México, a los 24 días del mes de agosto de 2018.

Dr. Horacio Flores Zúñiga
Secretario Académico

Mtra. Ivonne Lizette Cuevas Vélez
Jefa del Departamento del Posgrado

INSTITUTO POTOSINO DE INVESTIGACIÓN CIENTÍFICA Y TECNOLÓGICA, A.C.
IPICYT
SECRETARIA ACADEMICA

Acknowledgments

I want to express my sincere gratitude to my thesis advisor, for his fruitful academic and personal guidance and for the interesting discussions during the time that this work was developed, Dr. Florentino Lopez-Urías (FLU).

I must recognize my student colleagues M. C Juan Luis Fajardo, M. C Alejandro Cortez-Lopez, M. C Roque Sanchez Salas, Dr. Cristina Quintero, M. C Jose Olvera, M. C Cristina Corvera for the fruitful discussions about results and characterization techniques.

I am profoundly indebted with professors and technicians within the LINAN-IPICYT. Dr. Héctor Silva, Vicente Rodríguez, M. C Beatriz Rivera, M. C. Ana Iris Peña Maldonado, Dr. Gladis Labrada, and Dr. Mariela Bravo.

I want to thank Dr. Jose Luis Sánchez LLamazares, Dr. Armando Encinas Oropesa, and Dr. Emilio Munoz Sandoval for their valuable time in reviewing this thesis work.

Finally, I must recognize all the help, love, confidence and support from my family. A good part of the things that I achieved are because of their influence.

FLU thanks to Grant CONACYT Problemas Nacionales 2016-1-4148 and I also thank to Grant 220744 from CONACYT

Abbreviations

BCC	Cubic centered on the body
BZ	Brillouin Zone
CBx	Carbon nanotubes doped with boron
CNx	Carbon nanotubes doped with nitrogen
COD	Crystallography open database
CVD	Chemical vapor deposition
DOS	Density of states
DTG	Differential thermogravimetry
DWCNT	Double wall carbon nanotubes
EDS	Dispersive Energy X-ray Spectroscopy
EELS	Electron energy loss spectroscopy
ETEM	Environmental transmission electron microscopy
FCC	Cubic centered on faces
FFT	Fast Fourier Transform
FWHM	Width at half height
HOPG	Highly ordered pyrolytic graphite
ICDD	International diffraction data center
NCs	Nanocluster
NPs	Nanoparticles
PECVD	Plasma enhanced chemical vapor deposition
SAED	Selected area electron diffraction
SEM	scanning electron microscope
SWCNT	Single wall carbon nanotube
TEM	Transmission electron microscopy
WDS	Dispersive wavelength X-ray spectroscopy
XRD	X-ray diffraction
GO	Graphene oxide
RGO	Reduced graphene oxide

Table of Contents

General Remarks

1.1 General Objective

Synthesize and characterize nitrogen-doped multiwalled carbon nanotubes by the method of aerosol-assisted chemical vapor deposition using an inexpensive banded iron formation (BIF) powder as a catalyst to achieve a high yield production.

1.2 Specific Objectives

1. Characterize the as-received BIF powder.
2. Reduce the grain size of BIF powders by high-energy ball milling, varying the duration of grinding under an ethanol atmosphere.
3. Synthesize nitrogen-doped carbon nanotubes using the following catalysts: 1) pristine BIF powders; 2) ball milled BIF for 1 hour, 3) ball milled BIF for 2 hours and 4) ball milled by 3hours, by an aerosol assisted chemical vapor deposition.
4. Characterize the morphological, physicochemical and electrocatalytic properties of the as-produced carbon nanotubes grown on all of the BIF substrates.
5. Analyze the yield production of the carbon nanomaterial grew over the BIF catalyst.
6. Expose N-MWCNT samples to an acid treatment
7. Perform a heat treatment acid treated N-MWCNT to increase its surface area.

1.3 Hypothesis

- Banded iron formation is a material containing Fe oxides that could be reduced by thermal treatment at high temperatures with hydrogen gas. Therefore, this material could be used to fabricate N-MWCNTs. We are supposing that the additional content of BIF material could be very useful for increasing the yield.
- Ball milling could reduce the BIF ~~a~~ material to very small sizes, which considerably increases its surface area, this could improve the yield production of N-MWCNTs.

1.4 Justification

The catalyst is considered as one of the most expensive components to fabricate carbon nanomaterials. Therefore, to find an alternative cheap and effective catalyst for producing high-quality and high quantity of N-MCNTs remains a challenge for research and applications. Replacing expensive artificial chemical reagents by natural and abundant iron containing minerals could reduce costs of carbon nanostructures manufacturing. Also, N-doped carbon nanostructures promise high tech applications such as electrode or active material for energy production and storage, sensing and biosensing applications, electrocatalytic performance like OER and/or HER for instance. To the best of our knowledge nitrogen doping on carbon nanostructures using this type of catalyst remains unexplored. Any investigation that results in a decrease in production costs can lead to a breakthrough in the near future.

Abstract

Banded iron formation (BIF) powders are precambrian sedimentary rocks formed mainly by iron-oxide and silica. We have used BIF powders from the Bundelkhand craton located in the north of India as catalyst for the high production of nitrogen-doped multiwalled carbon nanotubes (N-MWCNTs) in an aerosol assisted chemical vapor deposition (AACVD) experiment. The N-MWCNTS were grown on BIF powders located inside the reactor at a temperature of 850 °C and under the presence of benzylamine (C_7H_9N) vapor as carbon and nitrogen source which was dragged by Ar/H_2 flow during 40 min. It was considered pristine BIF powder and those ball milling treated during 1, 2, and 3 h under an ethanol atmosphere. The BIF powders and N-MWCNTs sample morphology and composition profiles were analyzed by scanning electron microscopy (SEM), transmission electron microscopy (TEM), X-ray diffraction (XRD), X-ray photoelectron spectroscopy (XPS) Raman spectroscopy, and thermogravimetric analysis (TGA). BIF powder XRD characterizations revealed that this is formed by mainly formed by quartz and hematite as also confirmed by Raman spectroscopy. TGA measurements revealed that BIF powder subjected to a ball milling increases their weights as the temperature increases, suggesting a surface modification of hematite and quartz grains. It was found that the yield production and morphology of N-MWCNTs depend strongly of the BIF powder (pristine and those ball milled). Efficiency of 340 % wt./wt. for the yield production of N-MWCNTs was obtained for BIF powder ball milled during 1 h. The specific surface area of N-MWCNTs estimated by Brunauer–Emmett–Teller (BET) for the N-MWCNTs reached up to 275 m^2/g. The type of nitrogen doping (pyrrolic, pyridinic, quaternary), different nitrogen and oxygen functional groups (carbonyls, carboxylics, and nitrogen-oxide), Si species (SiO_2, SiO, Si^{4+}) and carbon species (sp^2 and sp^3) hosted at the surface of N-MWCNTs were quantified by the XPS characterizations. We have also investigated the electrochemical response of electrodes made of N-MWCNTs by cyclic voltammetry in order to assess the applications of our synthesized materials as energy storage and sensor systems.

Resumen

Los polvos de formación de hierro bandeado (FHB) son rocas sedimentarias de la era precámbrica, formadas principalmente por bandas de óxidos de hierro y sílice. Hemos utilizado polvos de FHB del cráter de Bundelkhand, ubicado en el norte de la India, como catalizadores para la producción de nanotubos de carbono de paredes múltiples dopados con nitrógeno (N-MWCNT) en un experimento de deposición de vapor químico asistido por aerosol (AACVD). Los N-MWCNTS se sintetizaron en polvos FHB colocados dentro del reactor a una temperatura de 850 ºC, bajo la presencia de vapor de bencilamina (C_7H_9N) como fuente de carbono y nitrógeno, que se arrastró por flujo de Ar / H_2 durante 40 minutos. Se consideró el polvo FHB prístino y el tratado por molienda de bolas durante 1, 2 y 3 horas bajo una atmósfera de etanol. Se analizaron los perfiles de morfología y composición de los polvos FHB y N-MWCNTs por microscopía electrónica de barrido (SEM), microscopía electrónica de transmisión (TEM), difracción de rayos X (XRD), espectroscopía fotoelectrónica de rayos X (XPS), Raman y análisis termogravimétrico (TGA). Las caracterizaciones del polvo FHB con XRD revelaron que está formado principalmente por cuarzo y hematita, como también lo confirma la espectroscopía Raman. Las mediciones de TGA revelaron que el polvo BIF sometido a una molienda de bolas aumenta su peso a medida que aumenta la temperatura, lo que sugiere una modificación de la superficie de la hematita y los granos de cuarzo. Se encontró que el rendimiento de producción y la morfología de N-MWCNT dependen fuertemente del polvo FHB (prístino y molido). Se obtuvo una eficiencia de producción del 340% en peso/peso de N-MWCNTs para polvo FHB molido durante 1 h. El área de superficie específica de los N-MWCNT estimados por Brunauer-Emmett-Teller (BET) para los N-MWCNT alcanzó hasta 275 m^2/g. El tipo de dopaje con nitrógeno (pirrólico, piridínico, cuaternario), diferentes grupos funcionales de nitrógeno y oxígeno (carbonilos, carboxílicos y óxido de nitrógeno), especies de Si (SiO_2, SiO, Si^{4+}) y especies de carbono (sp^2 y sp^3) alojadas en el la superficie de los N-MWCNT se cuantificó mediante las caracterizaciones XPS. También hemos investigado la respuesta electroquímica de electrodos hechos de N-MWCNT por voltamperometría cíclica con el fin de evaluar las

aplicaciones de nuestros materiales sintetizados como sistemas de almacenamiento de energía y sensores.

Chapter 1 - General Introduction

Carbon nanotubes (CNTs) are perhaps one of the most representative models carbon-based nanomaterials [1,2], for which many excellent properties have been described, and have already found a practical application. For example, in materials reinforcement, electronics, energy production and storage, catalysis and furthermore in fields such as medicine [3–6]. Different routes have been explored for increasing the production of carbon nanotubes such as the use of different catalysts, pre-fabricated or from natural sources (raw minerals extracted from the sea and mines, volcanic rocks, mud, among others).

Metals and metal oxides (MO) can be found in almost all natural materials. These are usually found in the form of small particles “natural nanoscale materials”, which are ideal to be used as catalyst in CNT synthesis. Depending of their chemical or physical properties at nanoscale level can produce exotic carbon nanomaterials with outstanding properties useful to many kind of devices and very likely for massive commercial uses [7]. For example, multi-branched CNTs were synthesized by Tao et al. [8] using as catalyst Cu/MgO containing an alkali-element. These carbon nanomaterials were proposed to be used in electronic devices at nanoscale level. Bacsa et al [9] fabricated MWCNTs using volcanic stones from the Greek island of Santorini as natural catalysts by CVD method. The source of carbon and oxygen was ethylene. The authors suppose that iron titanate crystals formed in the volcanic rocks catalyzed very thin MWCNTs.

In order to avoid the use of high quality artificial chemical reagents to fabricate MWCNTs Jipeng et al. [10] employed marine manganese nodule, which contains metallic elements, such as Mn, Fe, Cu, and Ni. For the carbon source they utilized acetylene gas. Endo et al, [11] considered that the fabrication of CNTs at great scale it is still a big challenge. For these reasons they used natural garnet as catalyst for producing large amount of this carbon nanomaterial. The carbon source in this case was city gas. They obtained 25-30% of the weight of catalyst as CNTs. They proposed that the air oxidation at 1000 °C the iron oxide in the garnet transforms to Fe_2O_3.

Su et al. [12] utilized natural lava as catalyst for CNT synthesis using a CVD process. In this case the as collected powder was crushed to be put inside the quartz tube. After that

the material was reduced with hydrogen during 2h. As source of carbon they used ethylene mixed with hydrogen and helium. The BIF powders contains around 11 wt.% of Fe_2O_3 also SiO_2 is present with 48 wt.%. Other phases as silicate phases and Fe–Ti oxides are also distributed in the material. The main product was carbon nanofibers with graphitic structure, but with irregular architecture. The diameters present a broad distribution since very small to large. The thermal stability is reasonable (550 °C).

Other natural resources are revised by Su, et al. as soil, garnet [13], bentonite [14], magnesite [15], forsterite, disposide, quartz, and brucite [16]. It is very important, to take into account these new strategies to convert waste to sustainable materials [17] to implement innovative routes to replace chemicals by natural or waste for promoting carbon nanomaterials [18]. For instance, see Figure 1-1 where you can see some of the aforementioned examples of carbon nanostructures synthesized on natural substrates.

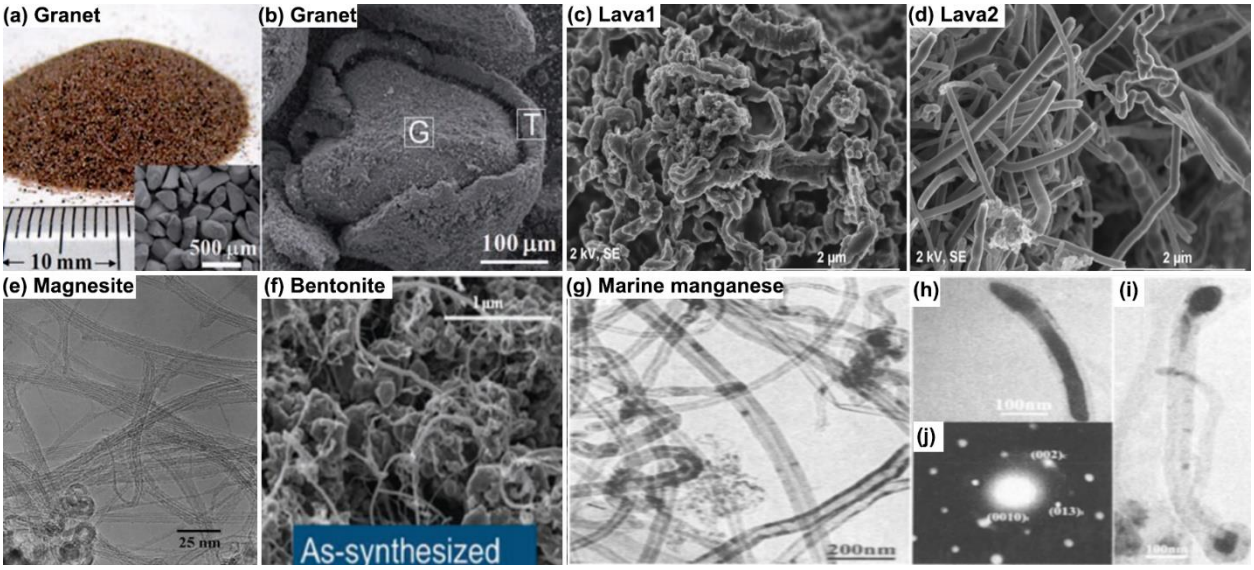

Figure 1-1 (a) Photograph of the garnet sand used to produce nanotubes; the inset is an SEM image showing the average diameter of the sand particles (average size ca. 200µm). **(b)** SEM image of the CNTs grown on the surface of the garnet sand particle (G and T indicate the garnet particle and CNT, respectively) [13]; **(c)** Lava1 and **(d)** Lava2 after the exposure of reduced lava to a C_2H_4 and H_2 mixture for 1 hour under different conditions [12]. **(e)** TEM image of SWCNTs grown on natural magnesite using a mixture of CH4 gas and Ar gas. **(f)** SEM image of as-synthesized CNTs/bentonite composite [14]. **(g)** TEM results aspects of as-synthesized CNTs, **(h)** encapsulated catalyst particle and **(j)** corresponding SAED pattern, **(i)** the catalyst particles encapsulated at both ends [10].

By discovering the real mechanism by the carbon nanomaterials growth, in particular of carbon nanotubes, it would allow us to control their quality and properties [19]. Such mechanism strongly depends of the precursors (catalysts, carbon source and dopant atoms) and the synthesis temperature. Therefore, they could be manufactured according to the medical, environmental, electronic or industrial application in general. Sometimes, the nature could be giving the answer to the role of some participant in the manufacture of carbon nanomaterials.

In this work, the fabrication of nitrogen-doped multiwall carbon nanotubes (N-MWCNT) using banded iron formation powders as catalyst is presented. The substrate material consists of natural and ball milled banded iron formation (BIF) from the India region, which play the catalyst role for producing the carbon nanomaterial. Our fabricated material is some kind of spongy with unexpected electrochemical properties. It is fabricated by using inexpensive banded iron formation (BIF) as catalyst which is a natural geological formation of earth.

It deserves to mention that Sakthivel, et al. produced fayalite by a mechano-chemical route using as starting material a low-grade iron ore and iron powder [20]. In this case the constituents of the silica-rich iron ore were hematite (54.2%) and quartz (44.6%) and other minority elements. However, Sakthivel and collaborators did not fabricated carbon nanomaterials with this material. Only one research group have fabricated MWCNT using as catalyst a combination of Fe and SiO_2. Shokry et al. [21] fabricated high yield of carbon nanotubes using some different catalysts based on iron and a mixture of iron and cobalt metal supported on SiO_2, Al_2O_3 or MgO. They found that yields as large as 2974 % could be obtained when Fe is combined with Al_2O_3 in a proportion of 40%-60% wt. respectively.

Chapter 2 - Experimental Methodologies

2.1 Instrumentation

All of the equipment used in this thesis belongs to the infrastructure of the Laboratorio Nacional de Investigaciones en Nanociencias y Nanotecnología (LINAN).

High energy ball milling was performed using the 8000D Mixer/Mill (SPEX SamplePrep) equipment (CLAMP SPEED 115V 1060cycles/minute).

Scanning electron microscopy (SEM) was performed using a FEI-HELIOS Nanolab 600 Dual Beam equipment, with a voltage of 10kV adding to the imaging an EDS detector and an electron back scatter diffraction orientation imaging camera. Small amounts of the as-synthesized material were deposited on carbon tape over aluminum pins prior to the observation. Measurements of CNTs diameter were obtained using ImageJ (free software for image analysis from the National Institutes of Health) from at least 5 SEM images of each sample studied.

High resolution transmission electron microscopy (HRTEM) was performed using a FEI Tecnai 300kV F30 STWIN G2 equipment, small amounts of the samples were ultrasonicated in ethanol and deposited over copper holey carbon TEM grids. The scanning transmission electron microscopy – high-angle annular dark-field imaging (STEM-HAADF) mode was employed.

X-ray diffraction (XRD) was collected using a Bruker XD8 ADVANCE diffractometer using a Cu K_α (λ=0.154nm) source. Data were collected at a scanning rate of 1°/min over the 2θ angular range of 10°-90°. Crystallographic Tool Box software was used to obtain zone axis analysis and diffraction patterns recognition, and Fullprof suite used for Rietveld refinement of the samples.

X-ray photoelectron spectroscopy (XPS) data were recorded with a PHI 5000 VersaProbe II spectrometer from Physical Electronics, equipped with a Monochromatic

Al Kα X-ray source (1486.7 eV) at 23.9eV of pass energy. The energy resolution was 0.6 eV. For the compensation of built-up charge on the sample surface during the measurements, a dual beam charge neutralization composed of an electron gun (≈ 1 eV) and an Ar ion gun (≤ 10 eV) was used. The recorded spectra were analyzed using CASAXPS software, and RSF database by peak fitting after Shirley background correction.

Raman spectroscopy measurements were carried out via Renishaw microRaman spectrometer using the 514nm laser excitation (lase power of 5.63mW) using an aperture of 20x. Laser spot size was ~1μm. Raman scattering was obtained at three different positions with an exposure time 50 s and spectral range of 100 cm^{-1} to 3500 cm^{-1}.

Single-point BET surface method is adopted to determine by N_2 adsorption the surface area and pore size distribution using a Quantachrome Instruments NOVA 2200e apparatus. Prior to the adsorption-desorption measurements, all samples were degassed at 200°C for 24 h.

Thermogravimetric analysis was performed using STA 6000 Perkin-Elmer equipment in a temperature range of 50–950 °C with a heating speed of 10 °C/min under dynamic flow of oxygen (20 mL/min).

Magnetometry was performed using the physical properties measurement system (PPMS) DynaCool Quantum Design at 300K.

Electrochemical properties were investigated by cyclic voltammetry in the standard three-electrode cell. A source meter Keithley 2400 was employed for the cyclic voltammetric (CV) measurements. A platinum wire served as the counter electrode, and an Ag/AgCl 3M electrode was used as reference electrode, H_2SO_4 0.5 M was used as liquid electrolyte. All measurements were made under ambient atmospheric conditions

2.2 Production of N-doped carbon nanotubes

The starting material for the current investigation comes from the Bundelkhand craton at north of India and consist of a banded iron formation (BIF) sample. BIF are sedimentary rocks composed of thinly bands, a typical BIF consist dominantly of hematite and magnetite grains alternating with quartz grain bands [22]. The sample labeled as “sb-21” has been characterized previously by means of electron microprobe study, reported Fe_2O_3 concentration in the sample is 52.71 wt.%, FeO concentration is 0.86 wt.%, while SiO_2 is 44.16 wt.% [23].

Figure 2-1 shows a schema of the process followed to obtain the carbon nanomaterial. BIF is a powder presenting a red-brown color as can be seen in Figure 2-1a. BIF are large rocks in the nature and it is necessary to crush it to be handle in small portions or powder. Ten milliliters of ethanol mixed with five grams of BIF powder was introduced into milling steel vials (6.4 cm high and 5 cm outer diameter and 3.3 cm internal diameter) with four steel balls (12.7 mm diameter) and other four smaller steel balls (6.33 mm diameter). The vials were strongly closed and put in the ball milling equipment for 1 h, 2 h, and 3 h (Figure 2-1b). Regardless of the time the resultant BIF powders exhibited sizes ranging from 150 -800 nm in diameter, showing a dark brown color (Figure 2-1c). Subsequently one-centimeter circular tablets of the four different BIF powders were fabricated using a 20-t press (Figure 2-1d). These small tablets were set inside the reactor in an aerosol-assisted chemical vapor deposition (AACVD) experiment (Figure 2-1e).

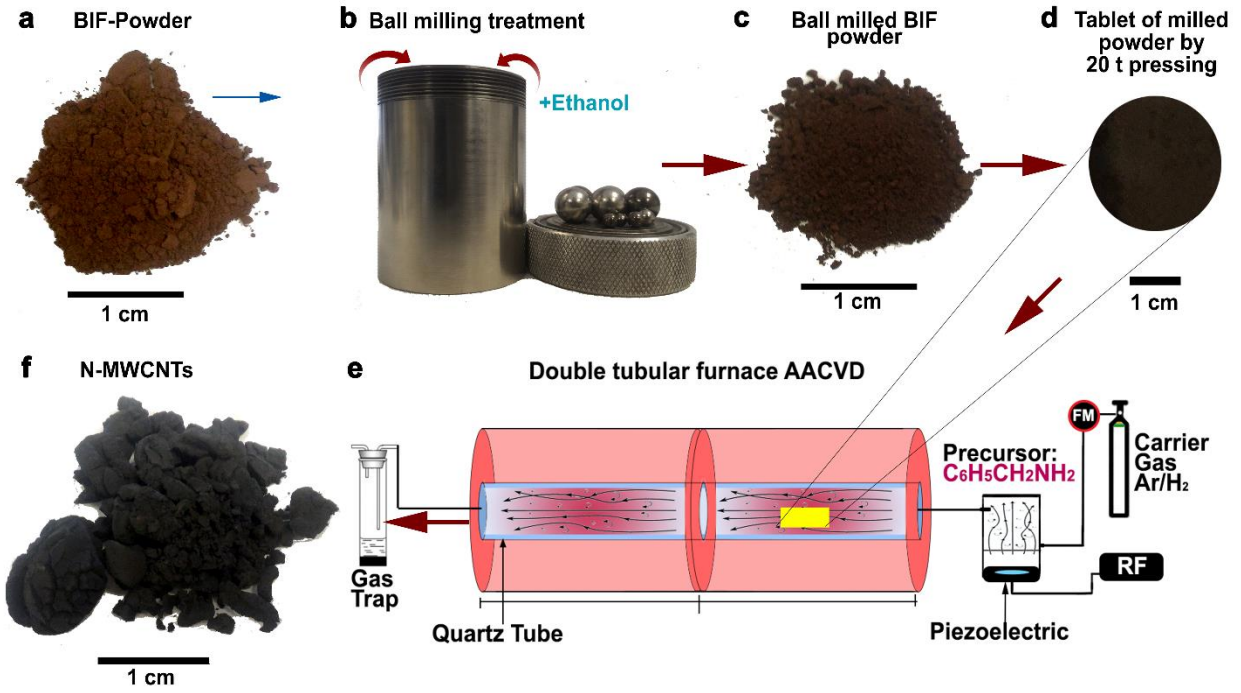

Figure 2-1 Schematic representation of the steps followed for the production of N-MWCNTs using banded iron formation (BIF) material as a catalyst. **(a)** As received BIF powder, **(b)** ball milling treatment of BIF powder under an ethanol atmosphere, **(c)** BIF powder after the ball milling treatment, **(d)** tablet made of milled BIF powder (1 inch diameter and 0.04 inch thichness) fabricated with a 20 ton press, **(e)** Aerosol-Assisted Chemical Vapor Deposition (AACVD) setup, here the N-MWCNTs grow on BIF tablets under a flow of benzylamine vapor at 850 °C, and **(f)** collected N-MWCNTs from the reactor.

The precursor solution was benzylamine (purchased from Sigma Aldrich ≥99.0%). The tablets placed inside the reactor (quartz tube) were exposed to a reduction process for 20 minutes at 850 ºC. A flow of 2.5 L/min H_2-Ar (5%-95%) carried out the nebulized precursor solution for 40 minutes. N-MWCNT sample is shown in Figure 2-1f. The carbon material obtained were labeled as S0, S1, S2 and S3 for samples grown over the ball milled BIF obtained after 0h, 1h, 2h and 3h of milling, respectively.

2.3 Oxidative functionalization and thermal treatment

Nitric acid (HNO_3 65%), sulfuric acid (H_2SO_4 98%) were supplied by Sigma Aldrich. All chemical reagents are analytical grade and were used as received. The procedures for modification of N-MWCNTs with acid treatment are done according to [24]. Briefly, 0.1 g of N-MWCNTs was immersed in 100 ml of H_2SO_4/HNO_3 mixture (3:1, v/v) at room

temperature for 30 minutes under continuous sonication. The solid obtained after filtration was black. Then it was washed several times with distilled water to reach a pH = ~7. Finally, was dried at 60ºC in a convection oven for 12 h. The resulting modified N-MWCNTs were used for further thermal treatments. Samples of ~0.1g of the acid treated N-MWCNTs-COOH were set in an electric furnace at 430°C for 12h. An alumina crucible of 10 ml was used in order to allow atmospheric oxygen exchange. Further dry under low vacuum conditions for 8 hours were performed for degasification before N_2 adsorption measurements. Figure 2-2 shows the scheme of surface modification of N-MWCNTs through acid and thermal treatments.

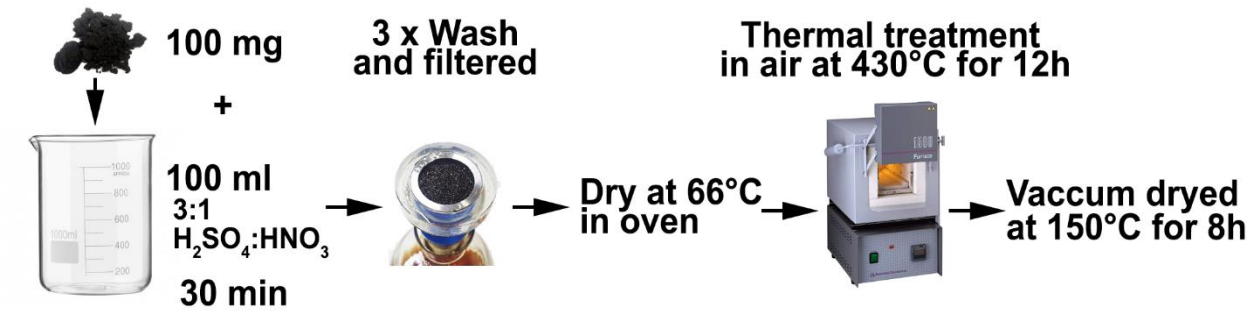

Figure 2-2 Schema of the procedures followed for N-MWCNT surface modification via oxidative functionalization and thermal treatments.

2.4 Electrochemical measurements

The electrochemical properties of the carbon nanotubes electrodes were investigated by cyclic voltammetry in the standard three-electrode cell. A source meter Keithley 2400 was employed for the cyclic voltammetric (CV) measurements. A platinum wire served as the counter electrode, and Ag/AgCl 3M was used as reference electrode. All measurements were made under ambient atmospheric conditions.

Chapter 3 - Results & Analysis

This chapter shows the results obtained in this research work whose results correspond to the characterization by SEM, TEM, XRD, XPS, Raman spectroscopy, BET analysis, TGA, magnetic and electrochemical analysis.

3.1 Characterization of ball milled BIF Powders

Figure 3-1a exhibits SEM images of as received (0h sample) and Figure 3-1(b-d) ball milled samples for 1 h, 2 h and 3 h, respectively. A uniform grain size could not be identified from these SEM images. The as received BIF powder exhibited grain sizes up to 40 µm. As the grinding time is longer the size of these grains decreases. The statistics illustrates that the most frequent size of samples are 284 nm, 209 nm, 229 nm and 143 nm for 0h, 1h, 2h and 3h samples, respectively (Figure 3-2a). Energy-dispersive X-ray spectroscopy revealed that 0h sample is composed mainly by O, Si, and Fe (**Figure 3-3**). XRD characterizations (Figure 3-1e) exhibits large peaks corresponding to the (104), (110) planes of Fe_2O_3 (hematite) phase [COD 96-210-1169] and the main peaks corresponding to (011) plane of the α-SiO_2 (quartz) phase [COD 96-101-1098]. Additional peaks around 2θ = 44.0 ° appeared in all ball milled samples, which are related with the (220), (102) planes of Fe_3C [COD 96-230-0092] and (101) plane of α-Fe crystallographic phases. The appearance Fe_3C was promoted by the ethanol in ball milling process. Table 3-1 shows the results of a Rietveld refinement of BIF powders, revealing the amount of the involved crystallographic phases. According to these refinements, the pristine BIF sample contains mainly 50.6 wt.% of Fe_2O_3, and 49.4 wt.% of α-SiO_2. Motivated by geological aspects, Singh et al. [23] investigated the composition of this BIF powder, they reported the hematite and quartz composition in accordance with this study.

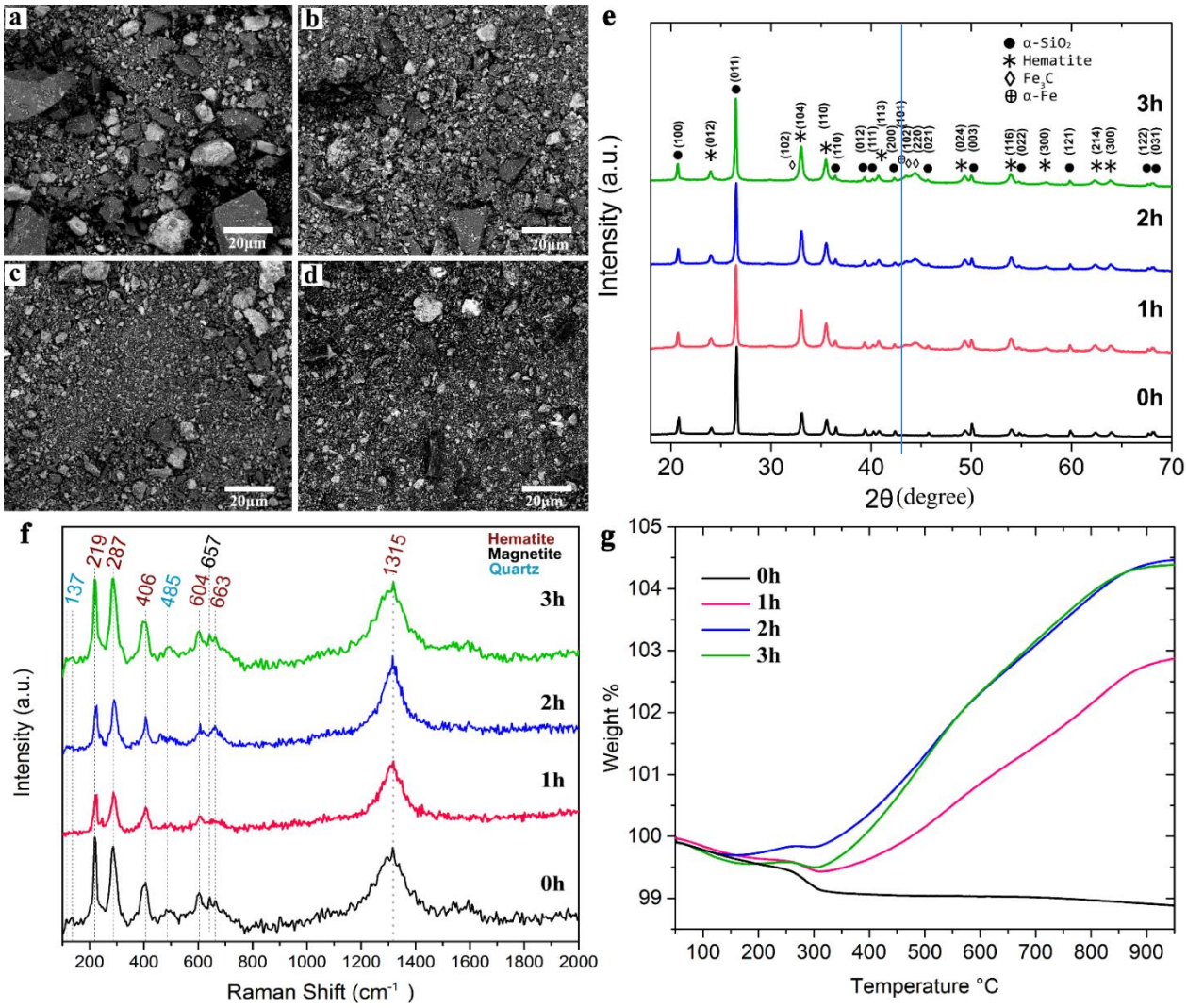

Figure 3-1 BIF powder characterizations (SEM, XRD, Raman spectroscopy, and TGA). Results for as received BIF powder (0 h) and those subjected to a ball milling treatment during 1h, 2h, and 3h. **(a)-(d)** SEM images, **(e)** XRD patterns, **(f)** Raman spectra, and **(g)** TGA measurements. From TGA results, a weight gain is observed (temperatures > 350 °C) for BIF powders subjected to the ball milling process, this behavior is likely due to the oxidation of quartz grains covered mainly by silicon or hematite nanoparticles covered by metals detached from the vial**.**

Raman spectra of BIF powders, confirmed the presence of the hematite structure (Figure 3-1f), the more relevant peaks at 219 cm^{-1}, 287 cm^{-1}, 406 cm^{-1}, 604 cm^{-1}, 663 cm^{-1} and 1315 cm^{-1} were identified [25]. The Raman peaks observed in 137 cm^{-1} and 485 cm^{-1} corresponds to the quartz [31]. An additional peak at 657 cm^{-1} was found, which could be

attributed to small traces of magnetite (Fe_3O_4) [25], the low peak intensity in contrast to the pronounced hematite Raman bands implies that there is only a low concentration of magnetite in the samples. Chourpa et al. associated the doublet 219 cm^{-1}-287 cm^{-1} from hematite to some micro-scale crystalline heterogeneity of the bulk iron oxide [27].

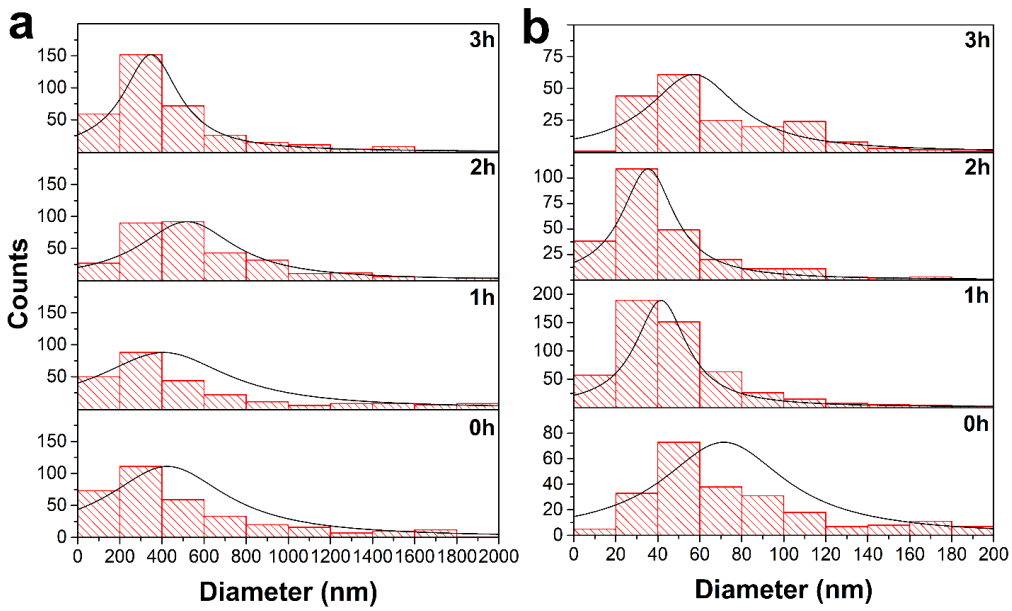

Figure 3-2 Histograms of measurements for (a) diameter particle of catalytic substrates and diameter of carbon nanotubes grown on the corresponding (a) catalytic substrate.

Figure 3-1g, displays the TGA results, all samples showed a loss weight for temperatures less than 180 °C. For temperatures in the range of 180-300 °C, ball milling BIF powder exhibited a slight increment of weight whereas pristine BIF powder experiences a progressive lost weight, reaching almost a loss of 1 % at 950 °C. The slight lost weight could be attributed to the removal of organic material. Interestingly, ball milled BIF powders experiences a gain in weight for temperatures greater than 300 °C reaching up to 4 % at 950 °C. The non-monotonous behavior of the weight vs temperature curves for ball milled BIF powders could be related to changes in the composition of the surface of hematite and quartz particles. Since the TGA measurement was performed under a dynamic flow of oxygen, it is expected that hematite and quartz with a surface rich in Fe, Si or their combination could capture oxygen and thus increase the weight sample. It is important to mention that in perfect (without surface composition modification) hematite

and quartz particles, the TGA curve should be a constant, not experiencing a lost weight. In order to illustrate this situation, we build several scenarios where oxygen from particles were removed, probably creating core shell nanoparticles as SiO_2@Si, SiO_2@FeSi, Fe_2O_3@Fe, and Fe_2O_3@FeSi (Figure 3-4). However, these circumstances must be studied in order to understand this phenomenon deeply, but this is outside of scope of this investigation. It is also possible the formation of Fe_2O_3@Fe_3C due to the ethanol atmosphere and carbon content in BIF powders. XRD results for TGA residuals obtained at 950 °C can be seen later in XRD results showing clearly the corresponding peaks of the hematite and quartz structures.

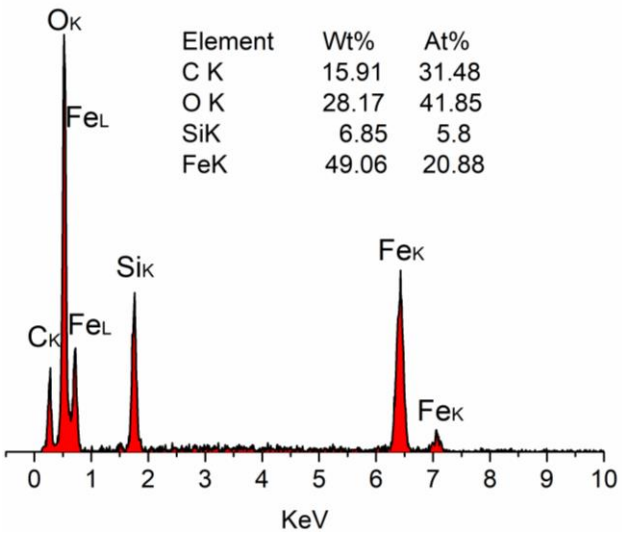

Figure 3-3. EDS spectrum of the pristine banded iron formation. Most of these peaks are X-rays given off as electrons returns to the K electron shell, except two that comes from Iron L shells

Table 3-1 Rietveld refinement for BIF powders. Fe_2O_3 (%) [96-210-1169]. α-SiO_2 (%) [96-101-1098]. Fe_3C (%) [96-230-0092]. Notice that Fe_2O_3 phase remains around 50 % whereas the α–SiO2 phase is affected by the milling time. The XRD patterns can be seen in Figure 3-1 (e).

Sample	Fe_2O_3 (%)	α-SiO_2 (%)	Fe_3C (%)	Av. Bragg R-factor	Final reduced chi^2
0 h	50.6	49.4	0	31.2	3.4
1 h	52.3	36.4	11.3	14.5	1.1
2 h	48.3	40.4	11.3	27.1	2.5
3 h	49.4	28.1	22.5	24.4	3.1

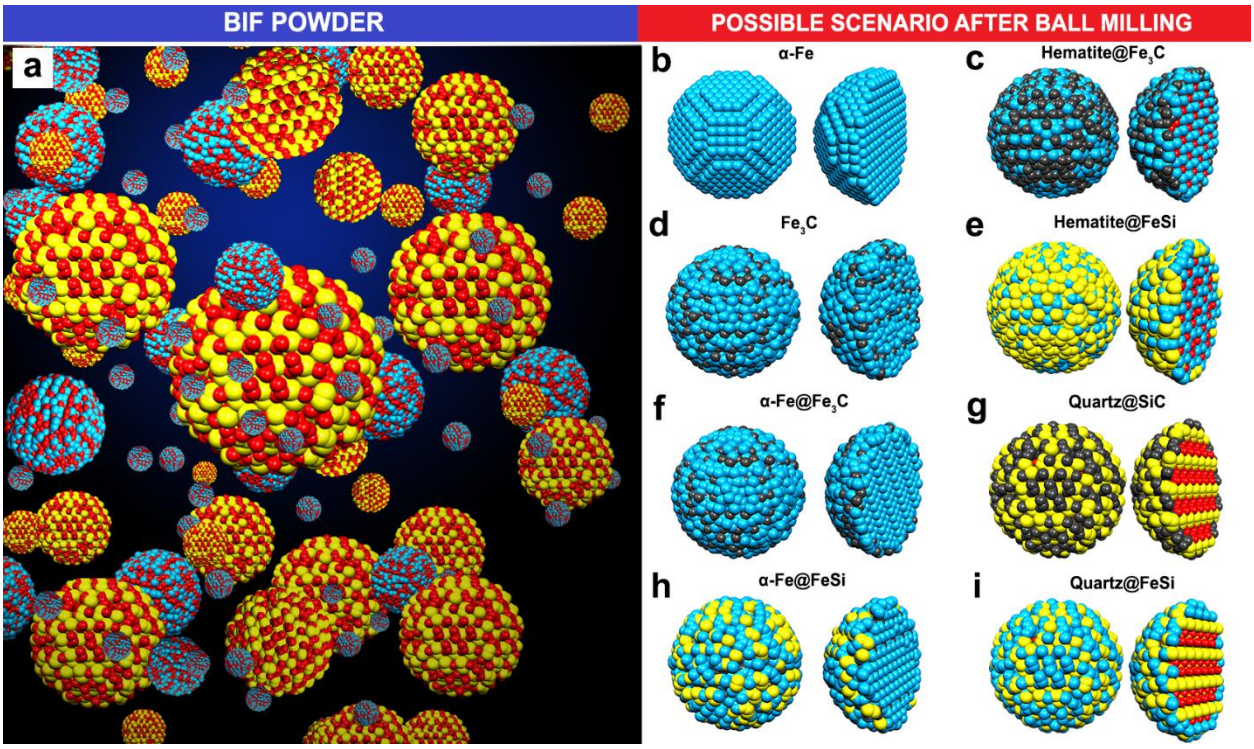

Figure 3-4 **(a)** Ball-and-stick model of BIF powder grains and **(b)-(i)** possible scenario after ball milling treatment. Color ball-and- stick atom refers to Fe (blue), O (red), Si (yellow), and C (black). The BIF powder is formed mainly by hematite and quartz particles (spherical shapes were used by facility). The ball milling treatment of BIF powder was carried out in presence of ethanol (C_2H_5OH).

It is also possible the formation of Fe_2O_3@Fe_3C due to the ethanol atmosphere and carbon content in BIF powders. XRD on the residual from TGA (Figure 3-24) was also performed, observing clearly the peaks corresponding to the hematite structure.

According Fernandez-Bertran [28] ball milling could be considered as a mechano-chemistry process where the bulk material can be reduced at very small sizes considerably increasing its surface area. It is also possible the formation of dislocations and point defects into the crystalline structure. From BIF powder XRD and SEM characterization, it is clear that the ball milling process modify the grain size and composition which will have important repercussions in the growth of carbon nanotubes as shown below.

BIF powders were used as a catalyst for growing N-MWCNTs, Table 3-2 depicts the initial amount of BIF powder, the final material inside the reactor (mostly N-MWCNTs), and the

efficiency of the catalyst in the production of N-MWCNTs. BIF powder ball milling during 1h showed the higher efficiency (~340 %). The different N-MWCNT samples were labeled S0, S1, S2, and S3 which were produced using pristine BIF powders and ball milled BIF powder for 1h, 2h, and 3h, respectively.

Table 3-2 BIF powders pristine and subjected to a ball milling treatment during 1 h, 2 h, and 3 h. The initial weight (w_1) refer to the amount of reduced BIF powder used in the synthesis of N-MWCNTs. The final weight (w_2) is the amount of product at the end of the AACVD experiment. The carbon deposit was calculated as $[(w_2-w_1)/w_1] \times 100$.

BIF-powder	Initial weight (w_1)	Final weight (w_2)	Carbon material (%)
0 h	0.237 g	0.907 g	282.54
1 h	0.221 g	0.973 g	340.27
2 h	0.425 g	1.417 g	233.41
3 h	0.353 g	1.040 g	194.11

3.2 Scanning Electron Microscopy

SEM images of N-MWCNTs corresponding to S0-S3 samples are shown in Figure 3-5. All of the samples exhibited non-uniform carbon nanotube diameters probably due to the particle size distribution determined for 0h-3h samples. It is important to point out, that the Fe-based nanoparticles are the catalysts of the carbon nanotubes [21]. For example, it was found that 0h powder with large grain size exhibited the largest N-MWCNTs diameters (Figure 3-2).

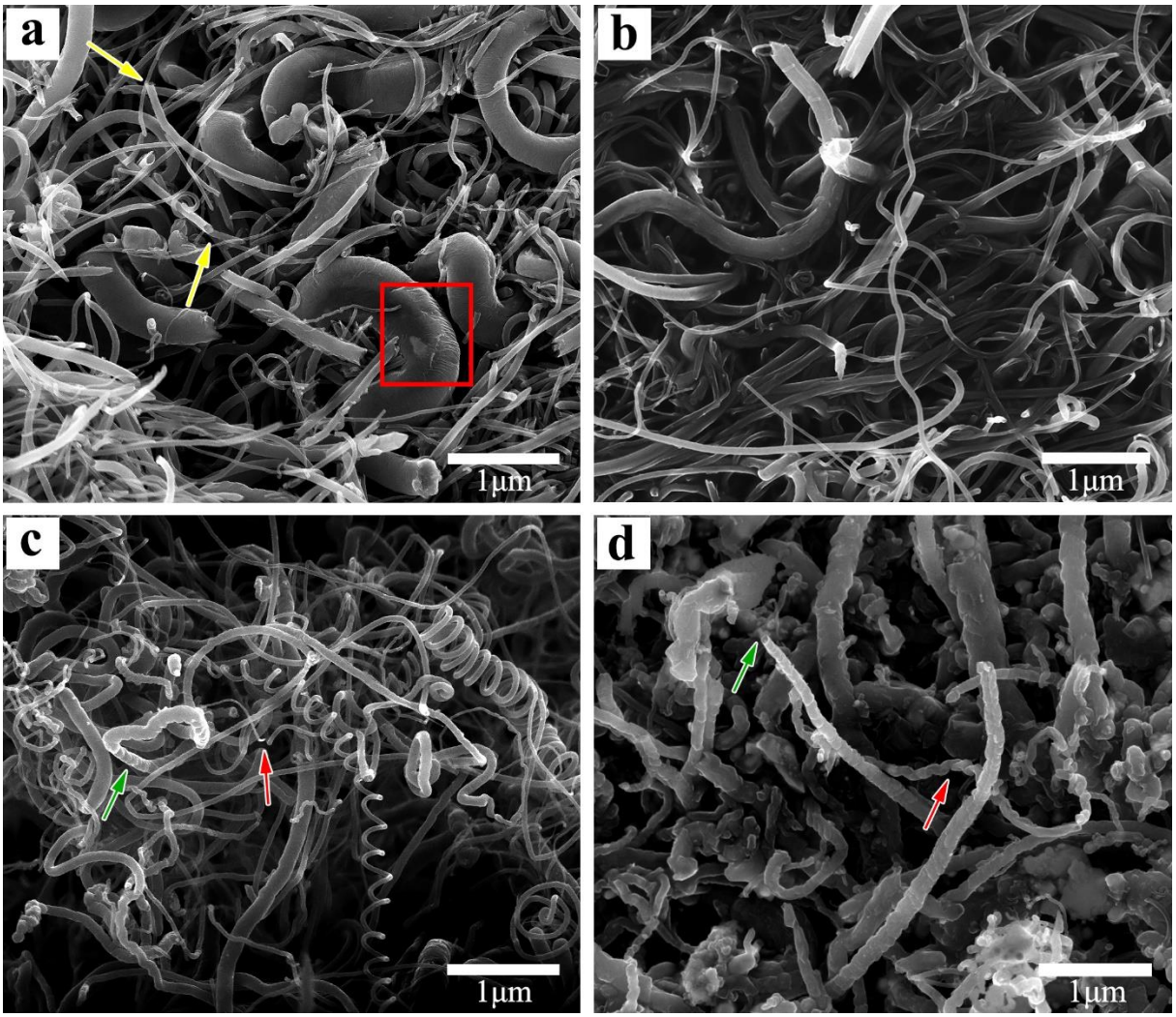

Figure 3-5 SEM images of N-MWCNTs grown on BIF powders. **(a)** As received BIF powder (sample S0). Samples S1 **(b)**, S2 **(c)** and S3 **(d)** correspond to N-MWCNTs grown on BIF powders subjected to a ball milling process during 1 h, 2h, and 3 h, respectively. Notice that the produced morphological shapes of N-MWCNTs depend strongly on the milling time.

Figure 3-5a displays N-MWCNTs grown using as received powder with a distribution diameter of 20-200 nm. Among other carbon fibers, few layered N-MWCNTs with small diameter were obtained (yellow arrows). We also observe large carbon fibers of ~800 nm diameter with a wrinkled surface (see red square). N-MWCNTs from sample S1 exhibited diameter of 20-60 nm with an aspect ratio >>1 (Figure 3-5b), this sample also exhibited coalesced carbon nanotubes along their walls (yellow arrow in Figure 3-7). N-MWCNTs from sample S2 showed smaller diameter nanotubes and different surface morphologies

(Figure 3-5c). N-MWCNTs with 200 nm of diameter exhibited a wrinkled or corrugated surface (green arrow), also it is possible to observe helical structures with different diameters. These helical morphologies could be formed due to the irregular shape of the catalytic particles [29]. The diameter distribution of N-MWCNTs is centered at 25 nm. Figure 3-5d shows the structure of N-MWCNTs from sample S3, here several morphologies can be appreciated with a corrugated and irregular surface [30]. Also, large aggregates were observed. Likely a long time of milling favored the coalescence of polycrystalline grains with different composition of the BIF powder, thus during the CVD experiment, these grains could hinder or perturb the normal growth of carbon nanotube. Additional SEM images of N-MWCNTs grown on BIF powders can be seen in figure (3-6 to 3-9).

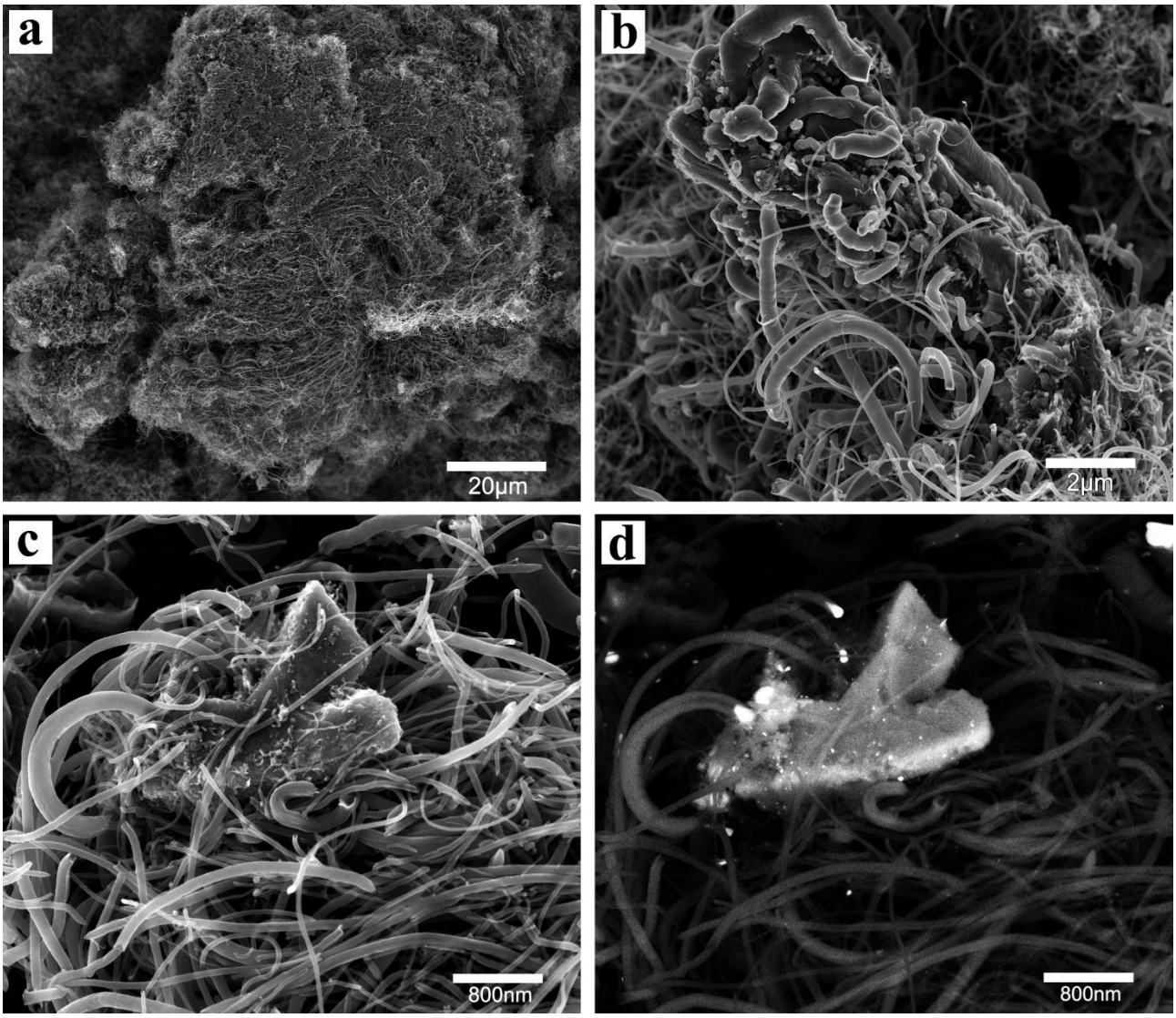

Figure 3-6 (a)-(c) SEM images of N-MWCNTs grown on as received BIF powder (sample S0). **(d)** Backscattering SEM image from **(c)**

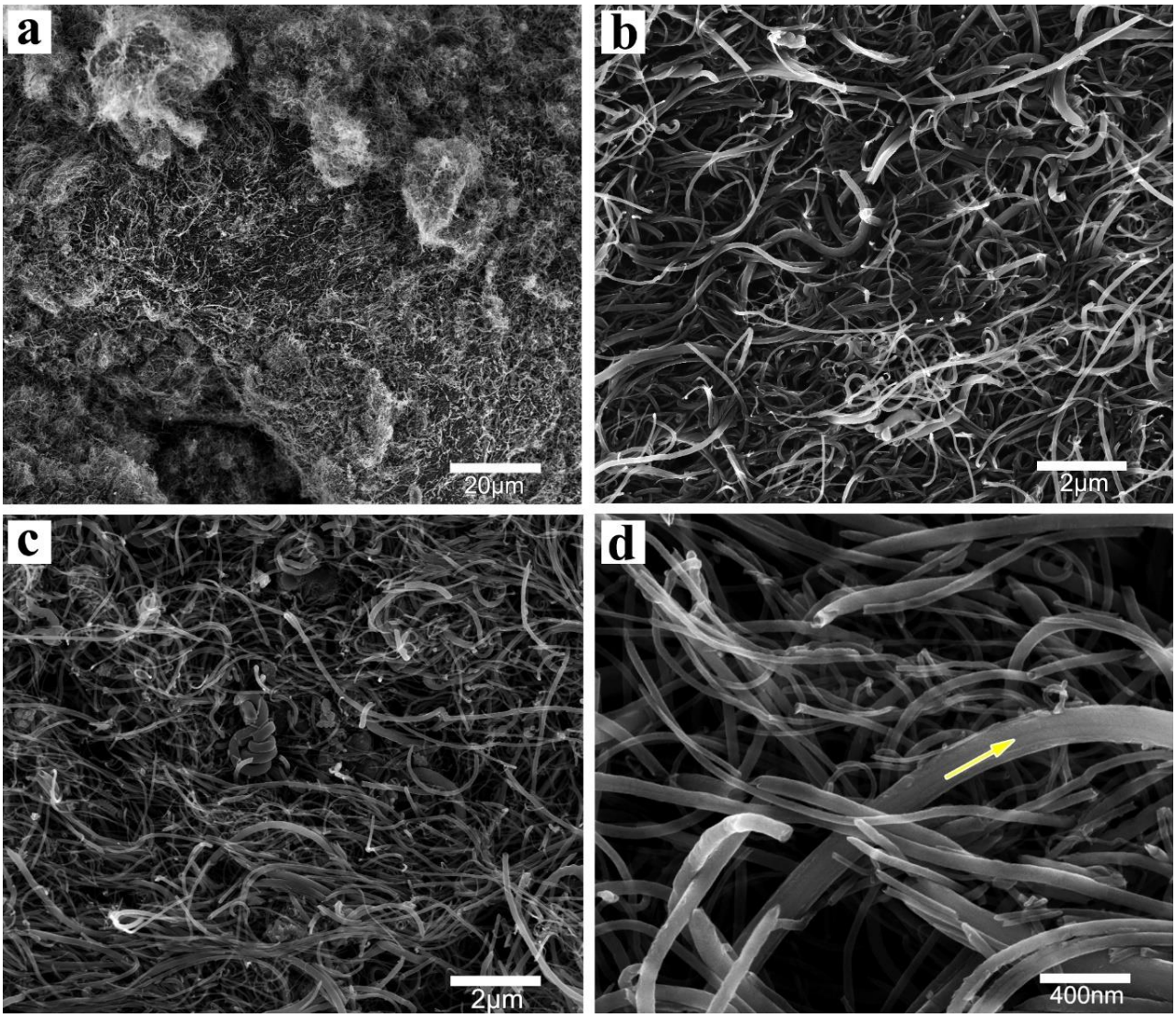

Figure 3-7 SEM images of N-MWCNTs grown BIF powder subjected to a ball milling treatment during 1 h (sample S1).

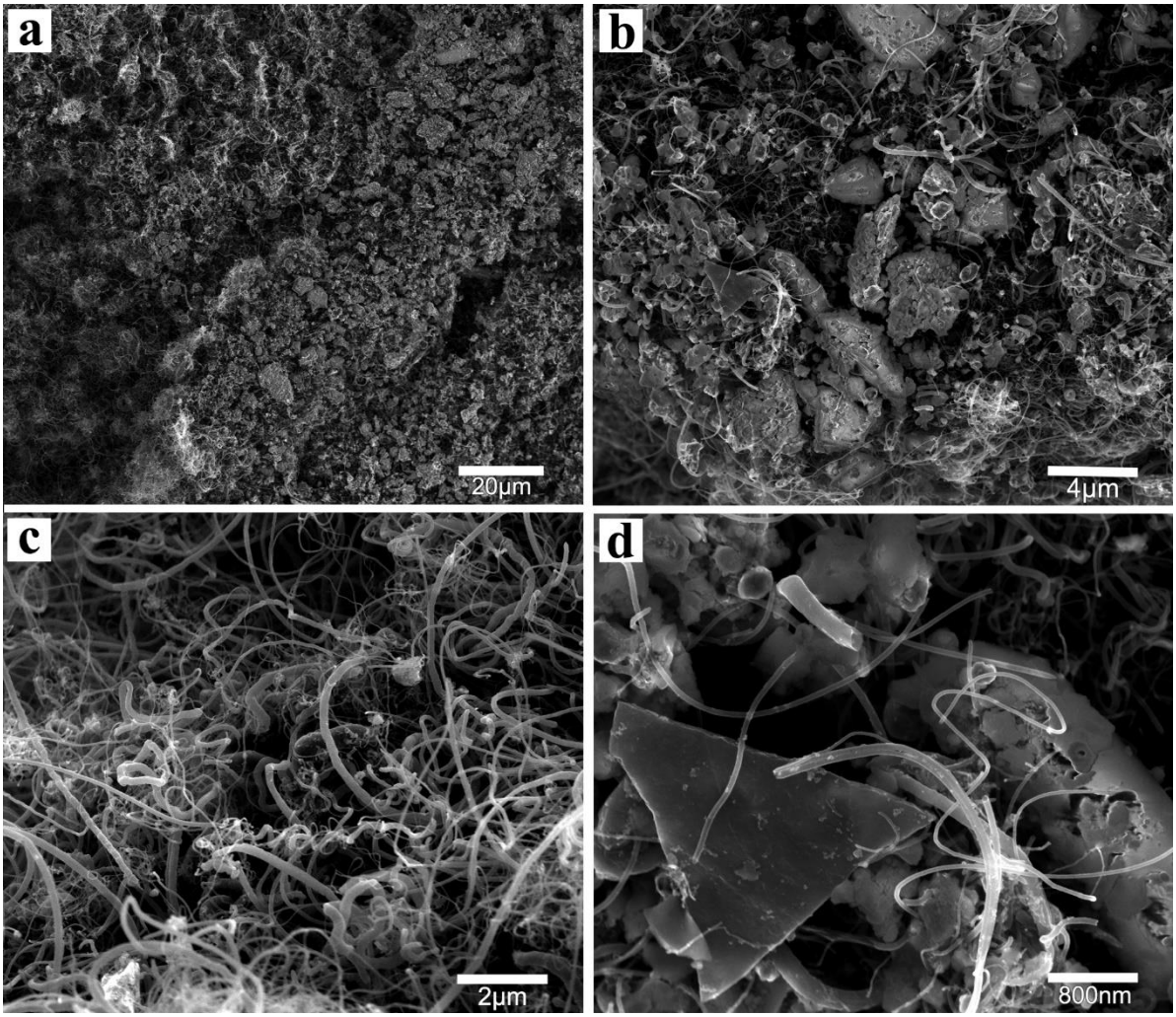

Figure 3-8 SEM images of N-MWCNTs grown BIF powder subjected to a ball milling treatment during 2h (sample S2).

.

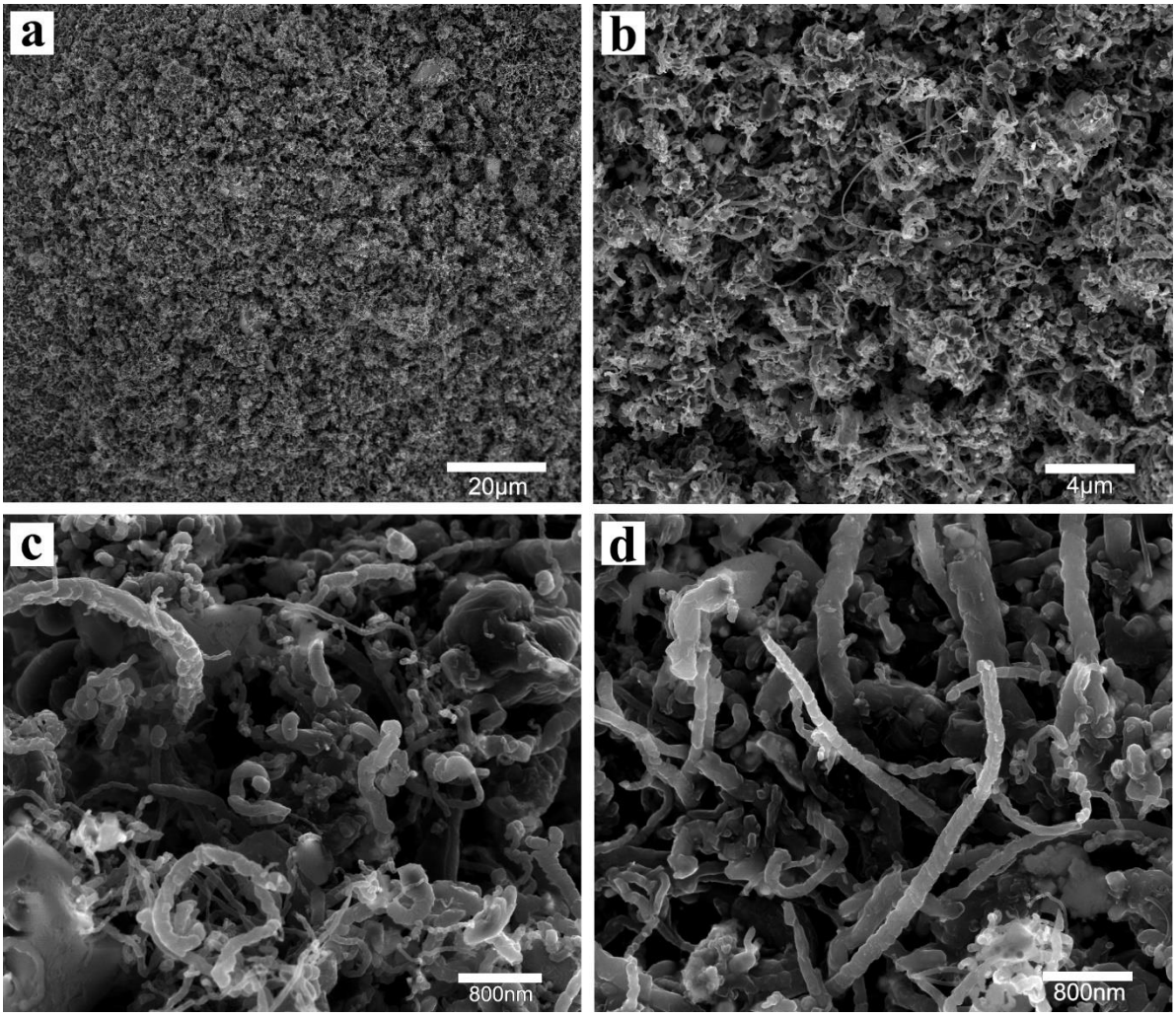

Figure 3-9 SEM images of N-MWCNTs grown BIF powder subjected to a ball milling treatment during 3h (sample S3).

3.3 Transmission Electron Microscopy

Figure 3-10 depicts TEM images of pristine BIF powder (Figure 3-10-d) and ball milled powder for 3h (Figure 3-10f-j). Pristine BIF powder shows irregular shaped consisting apparently in several agglomerated flat pieces. Notice the visible edges around the particle. It is also possible to see various lines as if the particle were constituted by several monocrystals. The crystal size is ~150 nm lateral dimension (Figure 3-10a).

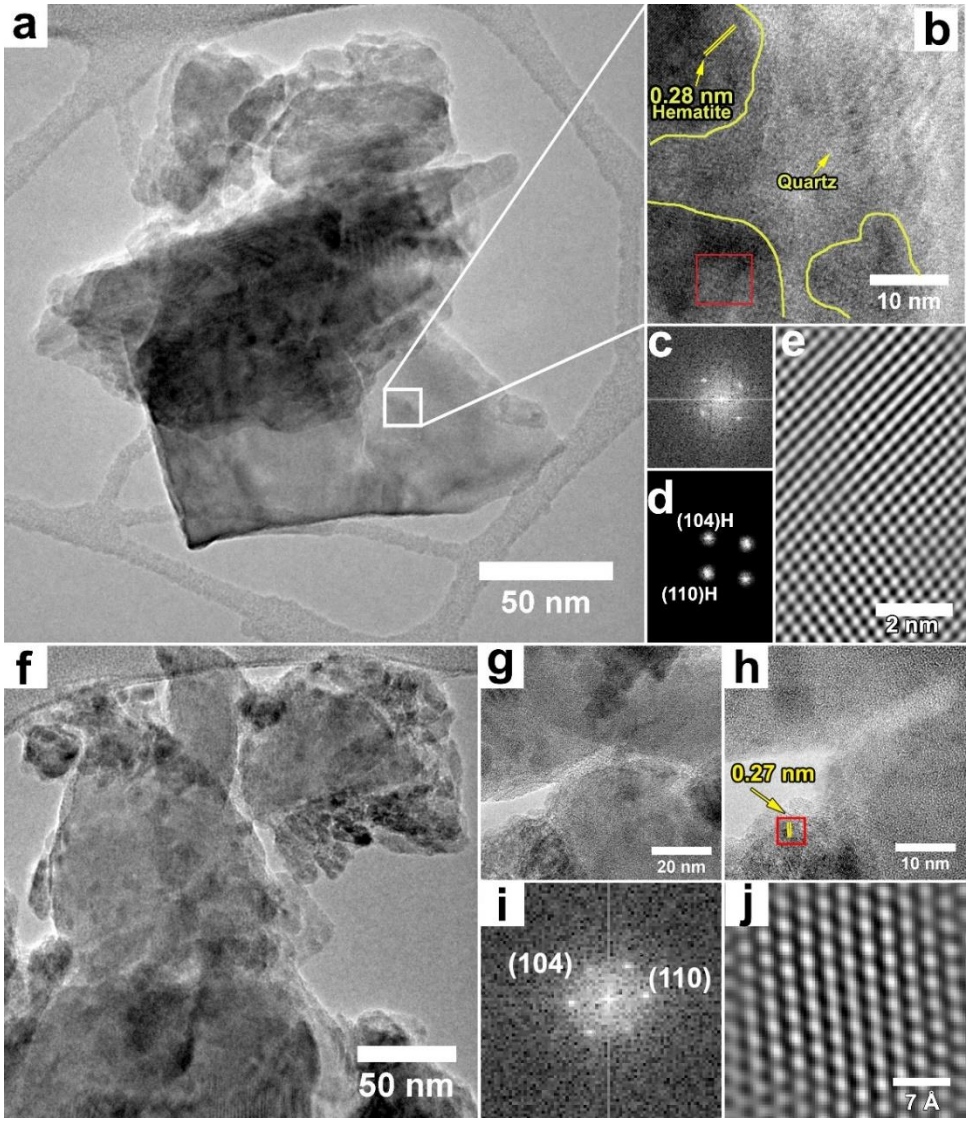

Figure 3-10 TEM and HRTEM image of as received BIF powder. **(a)** Quartz nanoparticle surrounded by hematite nanoparticles. **(b)** HRTEM taken from the enclosed area by the square in **(a)**, showing small hematite nanoparticles. **(c)-(e)** FFT analysis of the region enclosed in (b) showing an interlayer distance 0.28nm, plane (104). **(f)-(h)** TEM image of ball milling BIF powder for 3 h. **(i)-(j)** FFT analysis taken from the red marked square in **(h)** showing bright points corresponding to (104) and (110) crystallographic planes of the hematite crystal.

HR-TEM images of the flat particle (Figure 3-10b) illustrates an interphase combination of hematite and quartz where the yellow line indicates the grain boundary limits of hematite. The hematite (yellow lines) has an interplanar distance of 0.28 nm corresponding to the plane (104). Figure 3-10c and Figure 3-10d illustrates the FFT refinement over the red square in Figure 3-10b where two reflective directions are visible referent to the (110) and (104) plane of hematite. An inverse FFT analysis over these two directions is showed in Figure 3-10e. In the case of the 3h material (Figure 3-10f) is highly visible how these hematite-quartz agglomerates are distributed over a quartz matrix (Figure 3-12). Figure 3-10g depicts a section over the two quartz flat particles that are interconnected by an amorphous structure that can be part of a siloxane structure (Si-O-Si) or hydro siloxane structure (-OSiH_n). The crystalline structures anchored to the quartz matrix has an interlayer distance (yellow lines) of 0.27 nm, representative of a hematite structure. Through an FFT refinement (Figure 3-10i) over the red square in Figure 3-10h reveals the hematite phase planes (110) and (104) and the inverse-FFT over the principal planes (Figure 3-10j) observed the column of atoms of hematite.

Figure 3-11 shows TEM images of another particle of pristine BIF powder. It can be seen a polycrystal of about 1 micrometer decorated with smaller crystals as can be seen in high resolution in Figure 3-11b, the yellow lines show an interplanar distance of 0.25nm and 0.28nm in Figure 3-11c, corresponding to the plane (110) and (104) of the hematite phase.

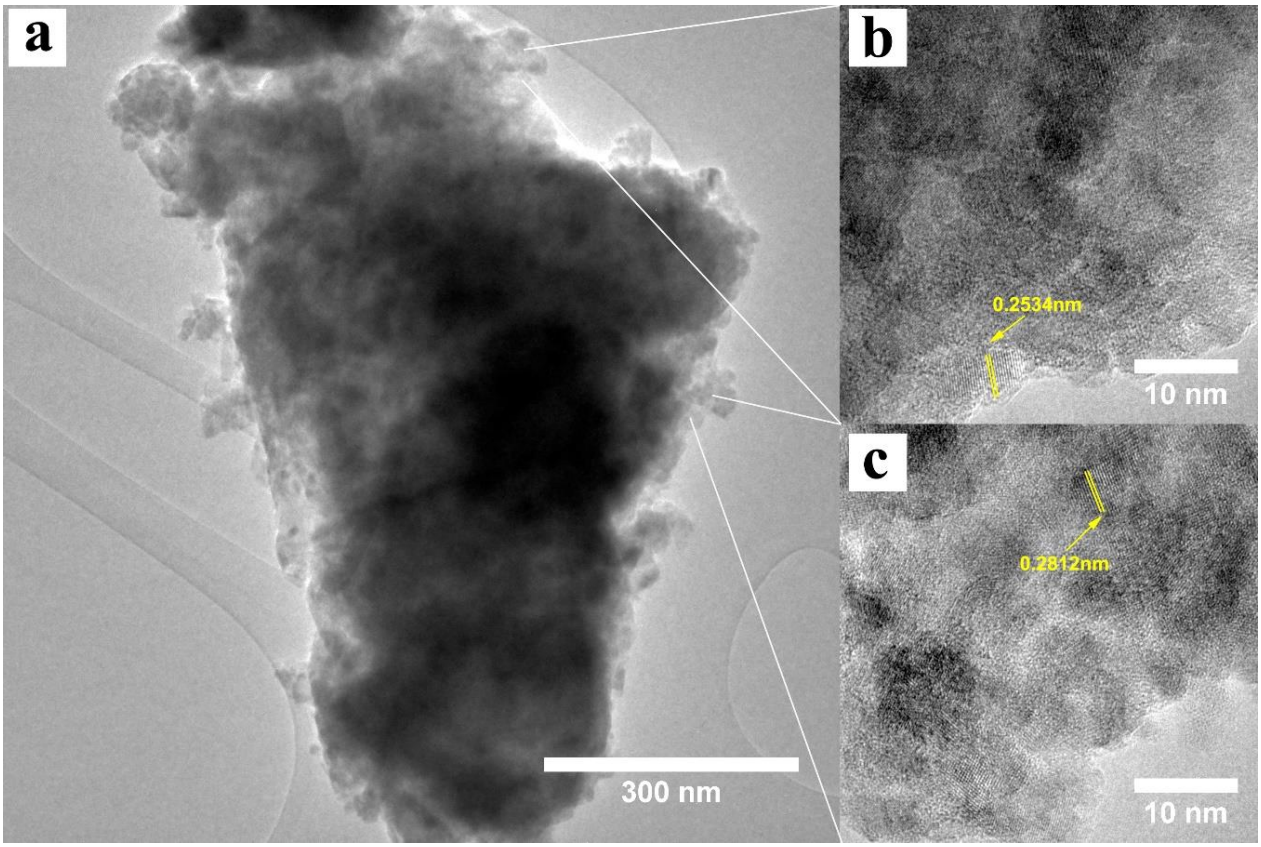

Figure 3-11 TEM micrograph of pristine BIF powder showing crystals aggregates; **(b)** shows HRTEM of nanoparticles of hematite on quartz displaying interplanar distance of 0.25nm, plane (110), **(c)** shows hematite nanoparticles with an interplanar distance of 0.28nm plane (104) of another zone of the larger crystal on **(a).**

Figure 3-12 exhibit contrast Z TEM HAADF imaging from BIF powder milled for 3h. It can be seen a particle decorated with smaller particles. Differences in contrast indicate that brighter tones correspond to heavier elements. This fact indicates the probability that the material that is seen with a light gray color is quartz and the particles brighter, metal particles, presumably Fe-based particles.

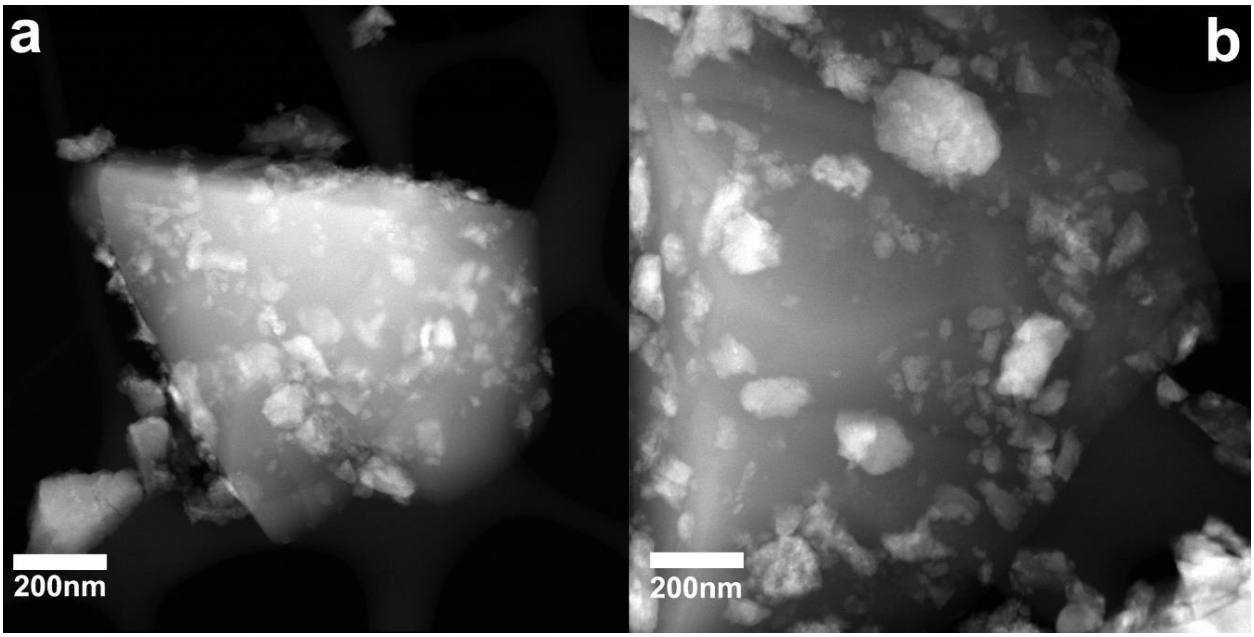

Figure 3-12 Contrast Z TEM micrograph of 3h milled BIF powder

Figure 3-13 displays different morphology aspects of carbon nanotubes grown using 0h material. As can be seen in Figure 3-13a, the carbon nanotubes present an irregular shape surface with a catalytic nanoparticle in one of its endings. This irregular architecture is probably motivated for two reason. The first could be related with the irregular shape of catalytic nanoparticle which is immerse in SiO_2 nanomaterial that can prevent a normal growing of tubular formation of N-MWCNTs. The second cause could be the interaction between nitrogen with silicon and oxygen atoms that inhibit their typical inclusion in the graphitic network. For example, Ai et al. found that the formation of such kind of irregular bamboo-structures is due to the encapsulation of Co and Mo_2C nanoparticles [31]. Figure 3-13b is an amplification of the tip of N-MWCNT where is clearly see the surface structure. Figure 3-13c is a high resolution TEM image showing the carbon layers and the distance between them.

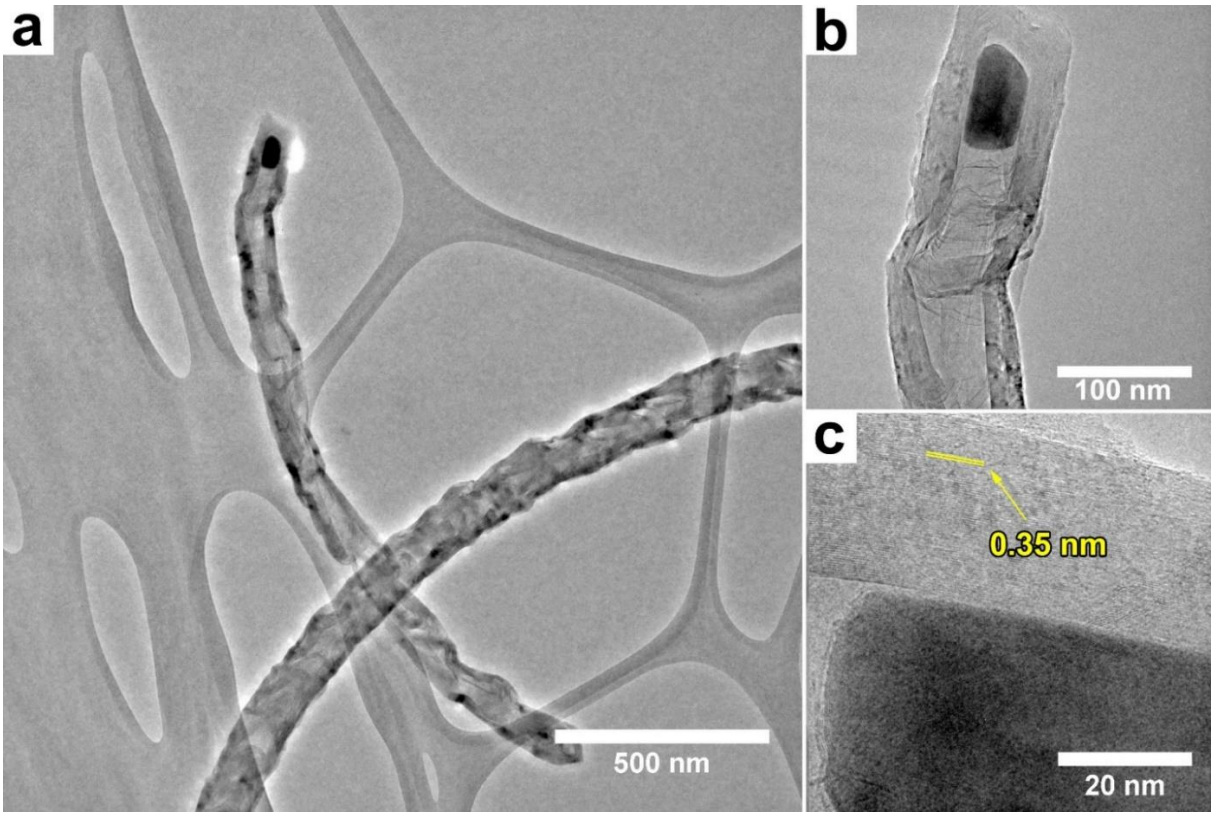

Figure 3-13 TEM micrographs of N-MWCNTs from sample S0. (a) This image show two carbon nanotubes with irregular bamboo shape morphology [31], consisting in a linear arrangement of hollow carbon pieces not uniformly assembled giving the appearance of a messy arrangement of cavities but following a certain direction; (b) this image exhibits the catalyst nanoparticle probably responsible of carbon nanotube growth; (c) high resolution TEM image of catalyst nanoparticle where it is possible to determine the distance between the carbon layers encapsulating it.

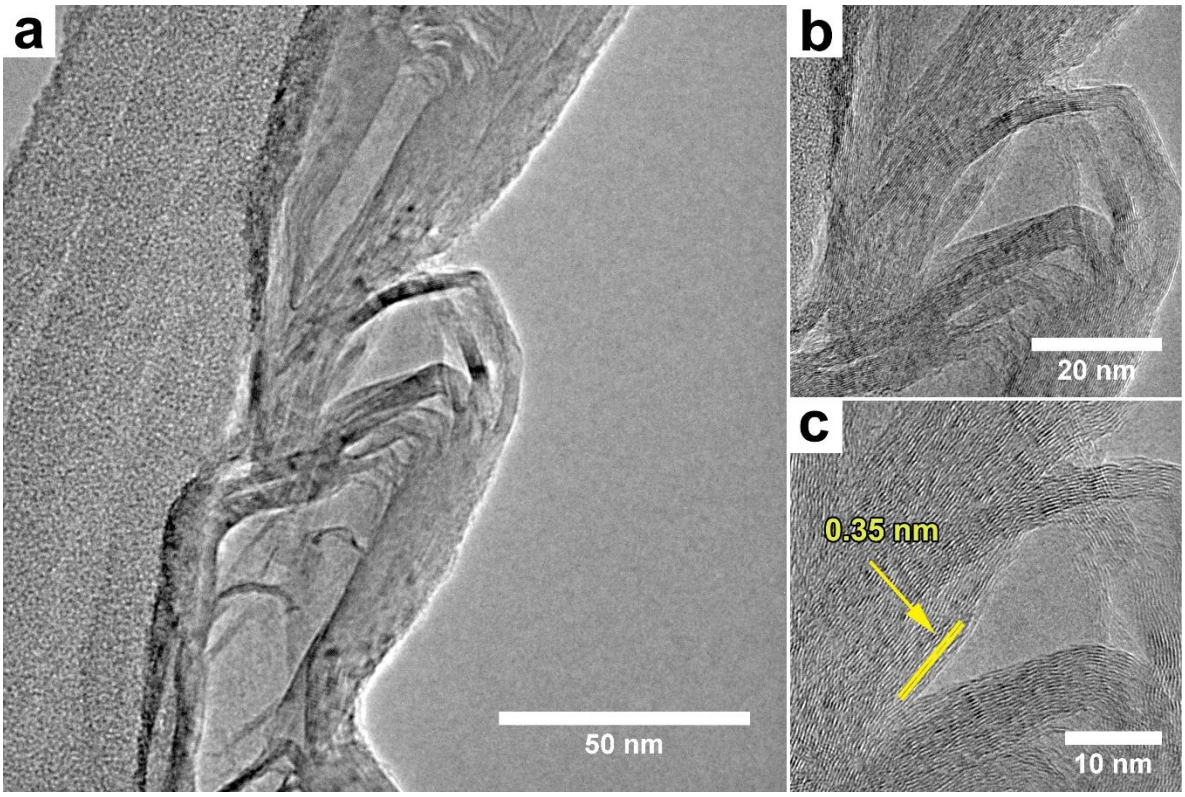

Figure 3-14 TEM micrograph of S0 N-MWCNTs milled BIF powder.

Figure 3.14. Shows a TEM image of N-MWCNT with nested conical bamboo shape, made by blended few layers graphene, figure 4-14c delineate an interplanar distance of 0.35nm, typical of graphite materials.

Figure 3-15 discloses several N-MWCNT of different sizes obtained from sample S1. There are two visible small diameter carbon nanotubes (10-20 nm) which are encapsulating catalytic nanoparticles at their tips. One of them (pointed out with a red arrow) is attached to a complex agglomerated of carbon and metal structures (see green arrow). Another 200 nm diameter N-MWCNT is evidently observed in this figure. The morphology is not typical nor simple, it has internal separated nanoparticles encapsulated in a carbon egg-shape structure [32]. Apparently, these architectures are assembled but not in a row. It seems that arrangement is like several heads (carbon egg-shape structure) conjoined with each other by tubular carbon formation. Each encapsulated nanoparticle presents a different morphology as can be seen in Figure 3-15b-d. This fact could be explained as a consequence of the ball milling process similar than the case S0, but with

the difference of crushing time and as consequence of that, the size of catalytic nanoparticles. For some unknown reason the silicon oxide nanomaterial although increase the yield also perturbs the normal growing of N-MWCNTs in this case.

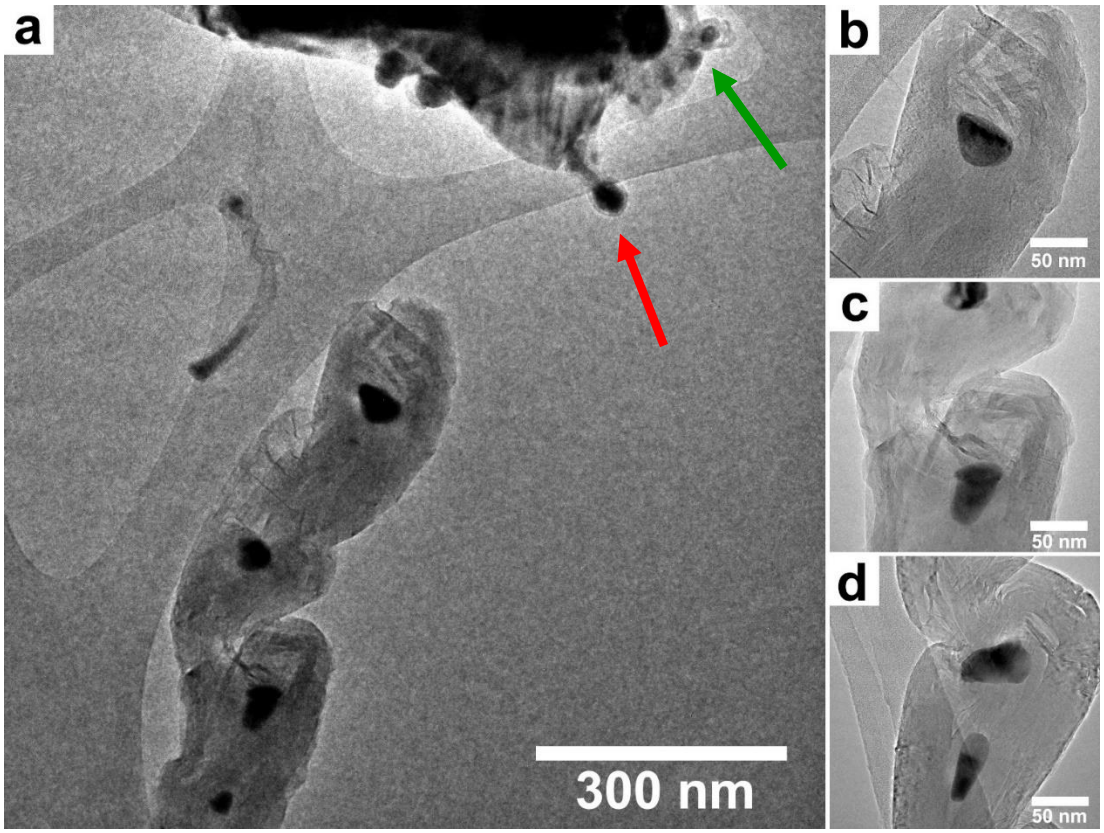

Figure 3-15 TEM micrographs of N-MWCNTs from sample S1. (a) This image shows a typical carbon nanotube with a very irregular bamboo shape morphology [32]. In this case, it seems that the total arrangement is built piece by piece, being a piece a carbon egg-shape structure (see (b), (c) and (d)).

Figure 3-17a exhibit a HRTEM image of Fe_3C nanoparticle encapsulated inside graphite material, located in sample S1, see figure 3-16a (red line). Figure 3-17d show a nanoparticle of alpha-iron with an interplanar distance of 0.20nm. Both particles where found in the S1 sample. Figure 3-18a show two N-MWCNTs from the S2 sample. The structure of one of them is curved and with a bamboo shape of the type nanotube-graphene hybrid bamboo-structure [33]. Notice that the surface of this CNT is curved but uniform. The other is straight but with curved zones (blue arrows). This kind of CNT exhibit a typical bamboo shape morphology. Figure 3-18d is a magnification of the yellow square of Figure 3-18c. Notice the strong stress in the internal curve (yellow circle). This effect

could be the reason that the distance between carbon layers is larger than 0.34 nm. In this external curve the distance between carbon layers was 0.36 nm.

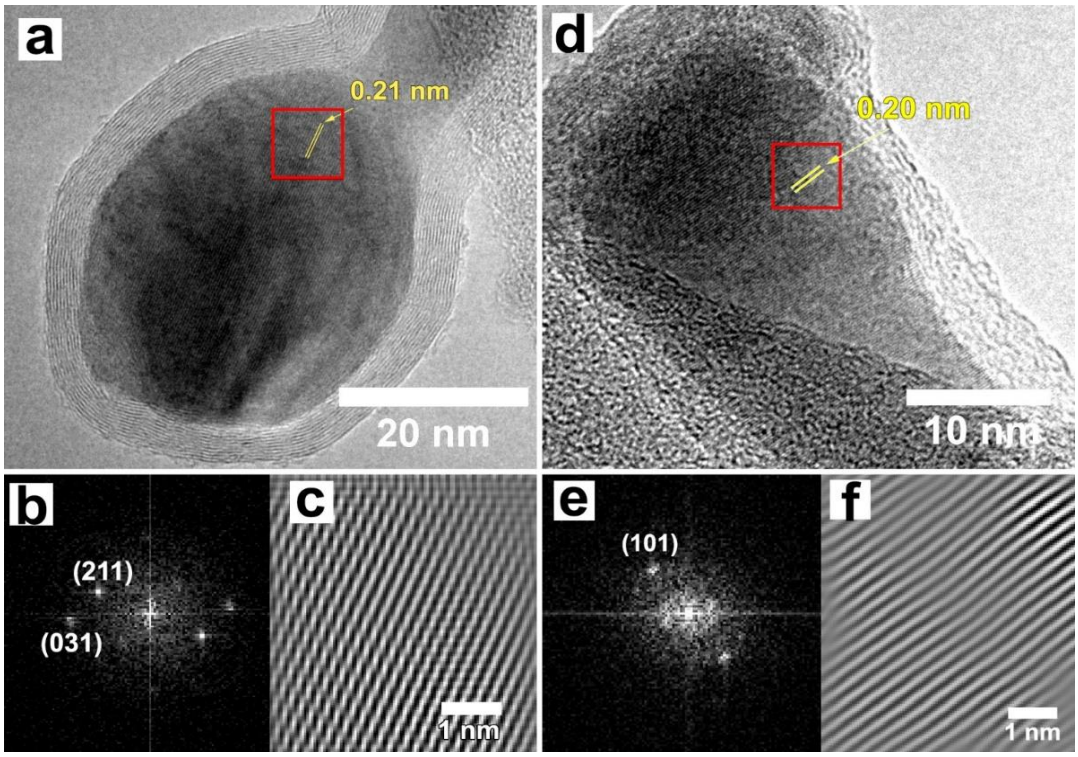

Figure 3-17 High resolution TEM images of Fe-based nanoparticles inside graphite materials. **(a)** Fe_3C showing an interplanar distance of 0.21 nm corresponding to the (211) crystallographic plane, **(b)** FFT pattern and the corresponding **(c)** Inverse-FFT analysis of the zone marked by red square in **(a)**. **(d)** α-Fe showing an interplanar distance of 0.20 nm corresponding to the (101) crystallographic plane, **(e)** FFT pattern and the corresponding **(f)** Inverse-FFT analysis of the zone marked by red square in **(d)**.

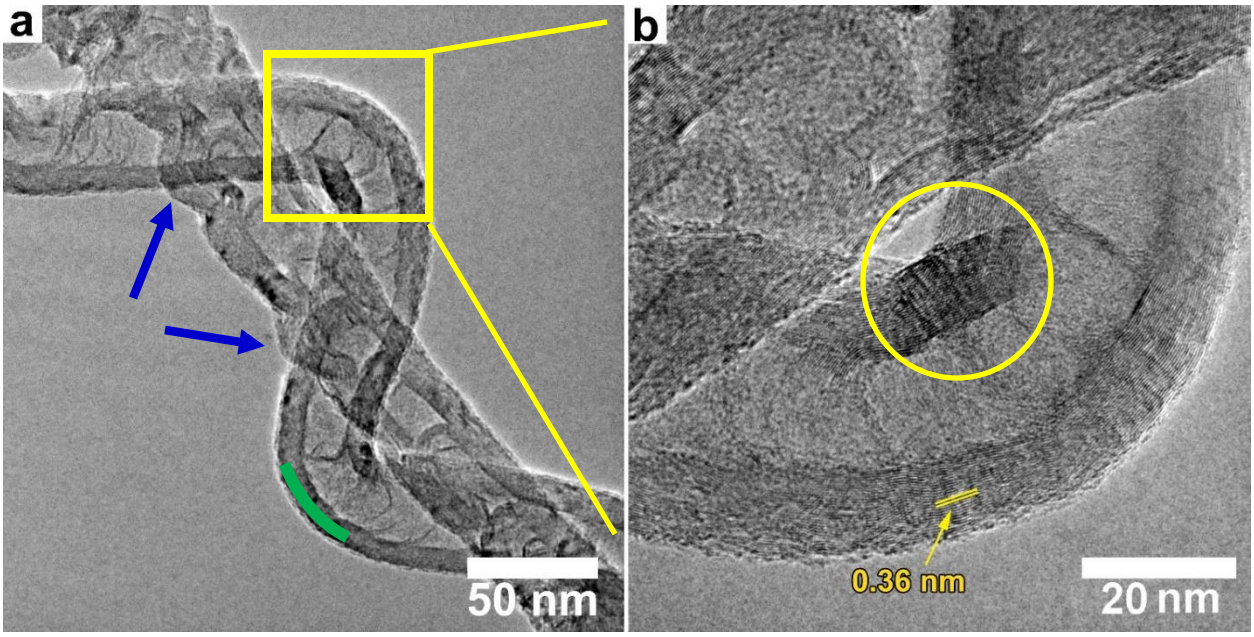

Figure 3-18 TEM images of two types of N-MWCNTs from sample S2. (a) This image shows a typical carbon nanotube with a very irregular bamboo shape morphology [33]**.** In this case, it seems that the total arrangement is built piece by piece, being a piece a carbon egg-shape structure (see (b), (c) and (d)).

Figure 3-19 depicts seven carbon nanotubes (four at Figure 3-19a and three in Figure 3-19b). In Figure 3-19a it can be distinguished four types of morphologies, namely one typical N-MWCNT (red arrow) presenting almost uniform separated graphene cavities; another (green arrow) apparently with normal bamboo shape segments, but with defective end or initial zone (yellow oval); a third example is a large diameter N-MWCNTs similar than the carbon egg-shape structures described previous lines (blue arrows); the last one is a complex small diameter carbon structure with double compartment arrangements (black arrow) following an almost longitudinal growing with double egg-shape structures. This diversity of morphologies here presented is a consequence of the ball milling time together with the incorporation of iron carbide from the steel vial used to crush the samples. Figure 3-19b also shows two typical bamboo shape morphologies one with graphene border for the cavities (blue arrow with and another with the typical conical compartments but showing intense stress in some small zones at its surface. The third N- MWCNT displays ~~with~~ irregular and small compartment with graphene-type separations [53].

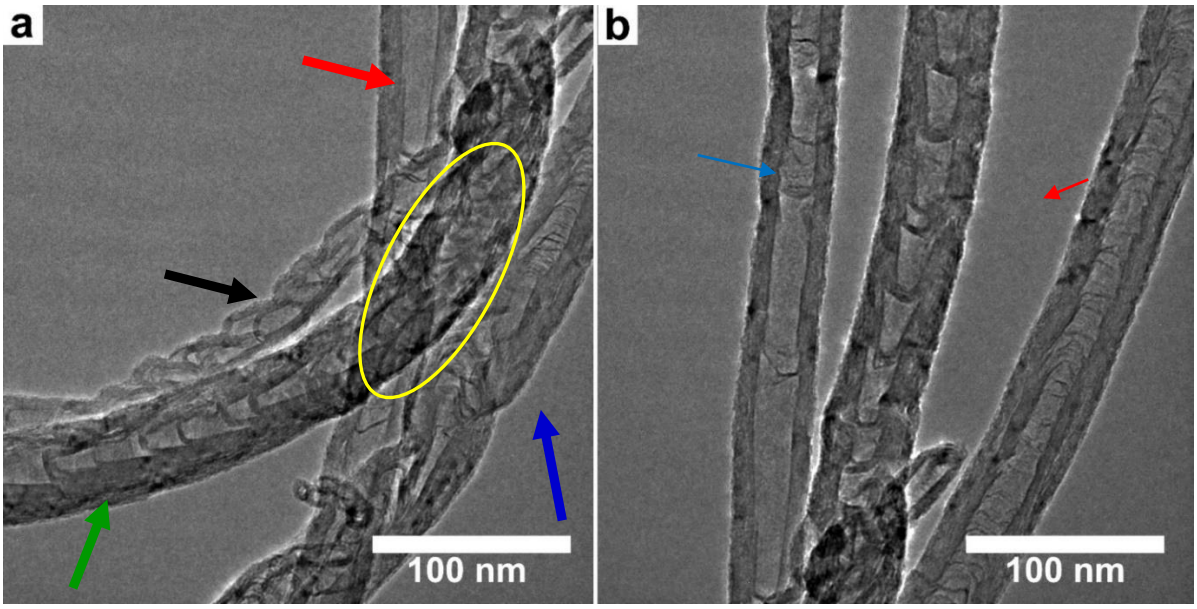

Figure 3-19 (a) TEM image of S3 sample with two bamboo shape N-MWCNTs morphologies (red and blue) and two unusual structures provoked by the composition nanoparticle sizes; (b) Three N-MWCNTs morphologies are already reported [29].

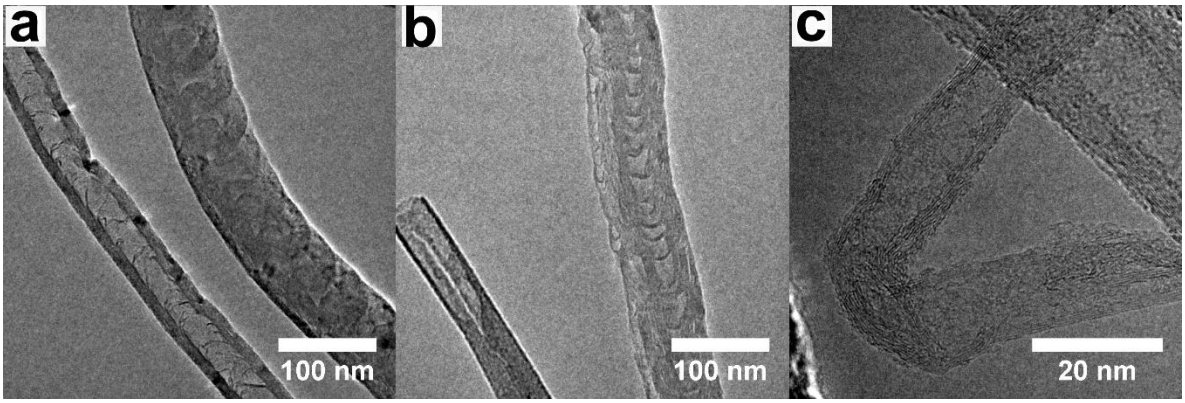

Figure 3-20 TEM micrograph of S2 N-MWCNTs milled BIF powder.

Carbon nanotubes with different internal compartments and few layers were observed for sample S2, see Figure 3-20(a,b). Five-layer carbon nanotube is shown in Figure 3-20c In general, the samples contain bamboo-like shape carbon nanotubes, complex carbon fibers with folding few layers graphite, and few layers carbon nanotubes. Therefore, these few layers carbon materials could be responsible of the large intensity of the 2D-band Raman peak as also reported by Ferrari et al [35]

Figure 3-21a exhibit other N-MWCNTs obtained from S3 sample. In this case the CNT is partial curved with a complicated internal morphology that is not possible to distinguish at this magnification. Figure 3-21b exhibit a magnification of the zone pointed out with the blue arrow nanotube with bamboo-shaped with a somewhat unusual morphology involving a inclined conical stacking sequence of the graphene sheets with intermittent hollow regions, similar of those observed by M. Nath et al. [34]. Figure 3-21c exhibits conical nested bamboo shapes; this structure may be promoted by agglomerates of catalytic particles. Figure 3-21d shows the end tail of the nanotube with an unusual bamboo morphology that resembles a scorpion tail.

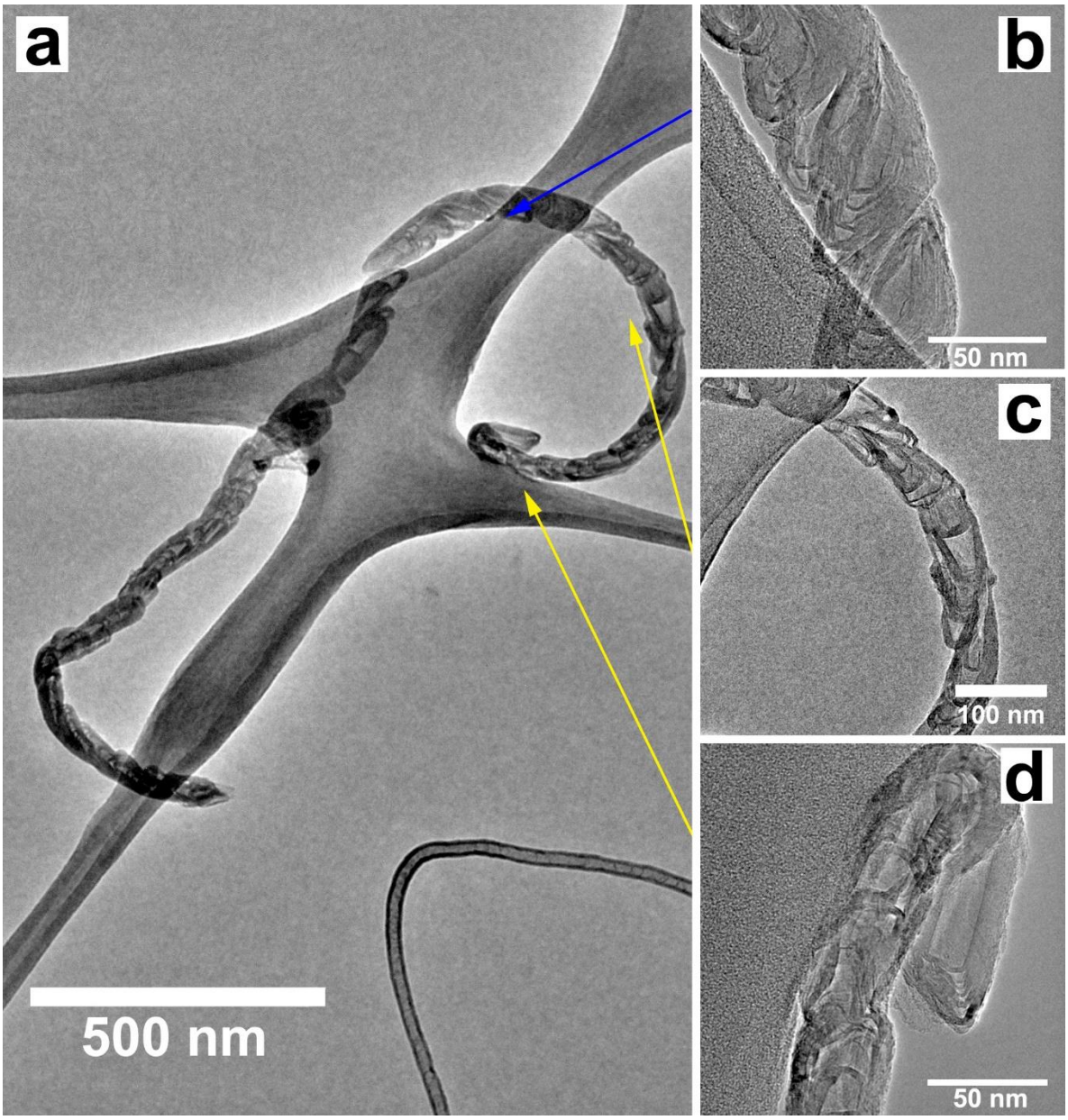

Figure 3-21 TEM micrograph of S3 N-MWCNTs milled BIF powder

3.4 X-ray diffraction

Figure 3-22 displays the XRD patterns of N-MWCNTs samples. We have plotted in two regions for clarity: 2θ=18-32 degrees (Figure 3-22a) and 2θ=32-72 degrees, the peaks that corresponds to quartz and graphite layered material can be observed The asymmetric and broad shape of the peak around of 2θ=26.5 involve the signals of the (002) crystallographic plane of graphite and (011) plane of α-SiO_2 [COD 96-101-1098]. A deconvolution analysis of this peak revealed the presence of the (002) plane of high oriented pyrolytic graphite at 2θ=26.47 degrees with an interlayer distance around 3.36 Å, the (002) plane of turbostratic graphite at 2θ=26.34 degrees with an interlayer distance round 3.44 Å, and the (011) plane of SiO_2 at 2θ=26.70 degrees with an interlayer distance of 3.33 Å (see Figure 3-23). The (100) crystallographic plane of α-SiO_2 [COD 96-101-1098] was also identified in 2θ=21.0 degrees. The main peaks corresponding to Fe_3C [COD 96-230-0092] and α-Fe [COD 96-900-6596] were identified (Figure 3-22b). Notice that after CVD synthesis of N-MWCNTs, no signals of Fe_2O_3 (hematite) were observed, suggesting that Fe_3C particles are formed as results of a reduction of Fe_2O_3 hematite particles during the CVD experiment.

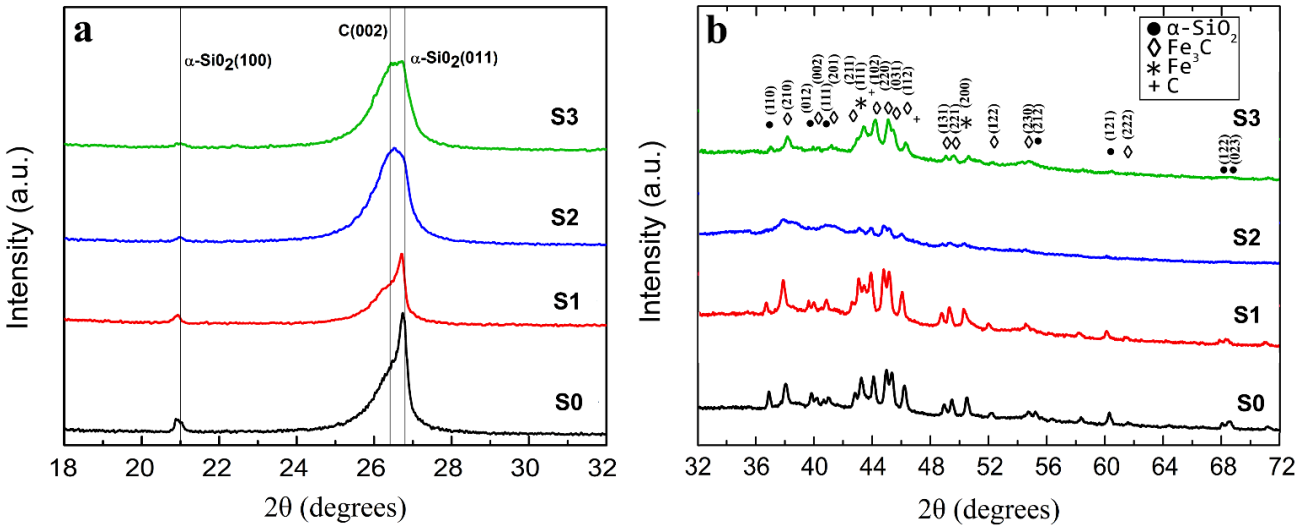

Figure 3-22 XRD patterns for N-MWCNTs grown on BIF powders containing Fe_2O_3 (hematite) and α-SiO_2 (quartz) divided into two regions for clarity: **(a)** 2θ=18-32 and **(b)** 2θ=32-72. Results for N-MWCNTs grown on as received BIF powder (S0) and N-MWCNTs grown on BIF powders subjected to a ball milling process during 1h (S1), 2h (S2), and 3h (S3). The C(002) peak typical of graphite materials was clearly identified. The presence of quartz and Fe_3C (iron carbide) crystal phases were also observed. Notice that the presence of hematite is no longer observed due to the reduction process during the first minutes in the AACVD experiment. A deconvolution analysis in the region of 2θ=24-28 degrees is shown in Figure 3-23 and Table 3-4.

Table 3-3 Rietveld refinement for synthesized nanocarbons. Graphite (%) [96-901-2706]. α-SiO_2 (%) [96-101-1098]. Fe_3C (%) [96-230-0092] and α-Fe [96-900-6596]. The XRD patterns can be seen in **Figure 3-22**.

Sample	Graphite (%)	α-SiO_2 (%)	Fe_3C (%)	α -Fe	Av. Bragg R-factor	Final reduced chi^2
0 h	61.70	27.5	8.70	2.10	31.2	17.1
1 h	43.02	45.29	9.58	2.11	14.5	12.9
2 h	48.64	39.76	9.8	1.8	27.1	12.5
3 h	71.4	14.4	12.8	1.5	24.4	8.1

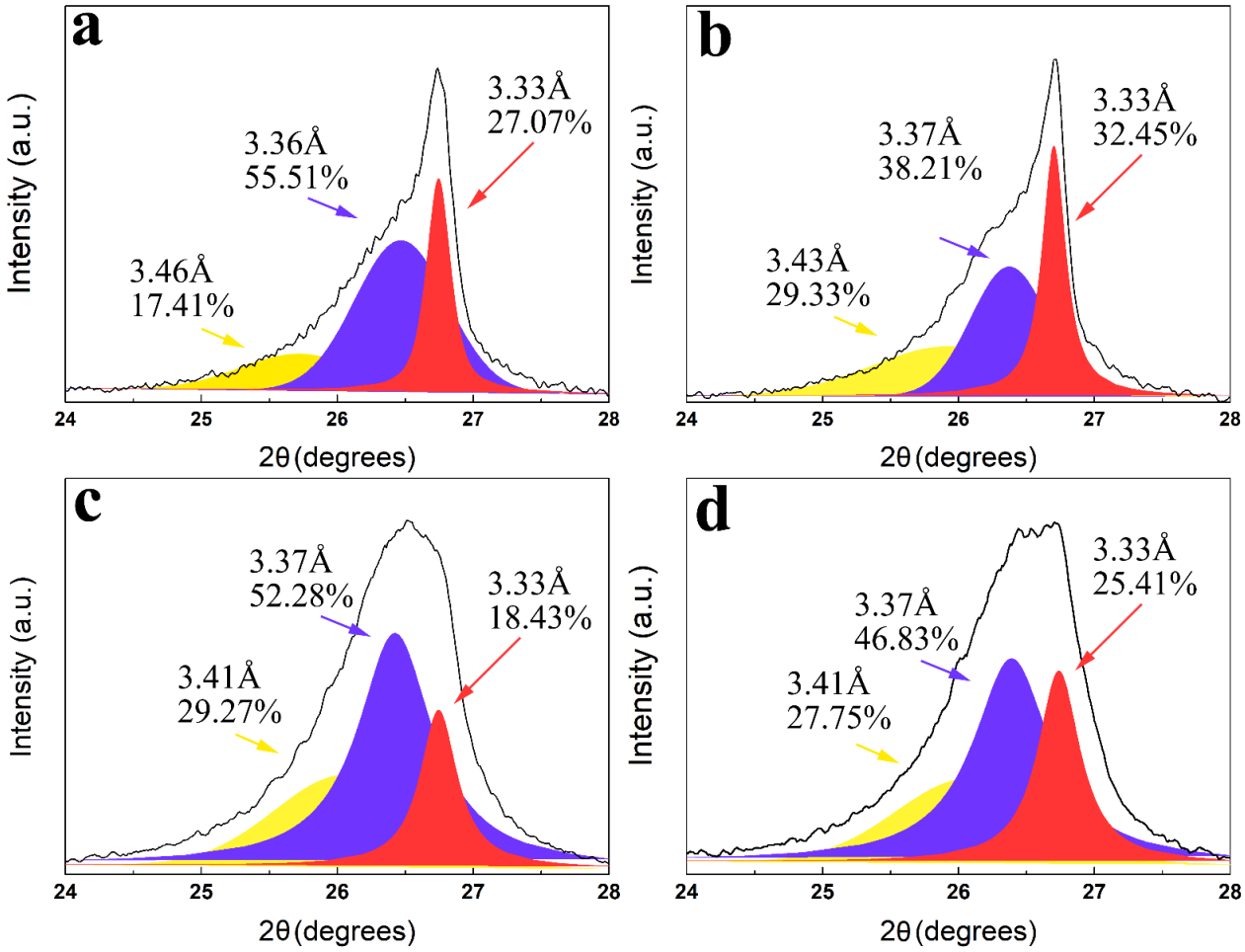

Figure 3-23 Deconvolution of the asymmetric XRD peak in the range of 24-28 degrees for N-MWCNTs grown on: **(a)** as received BIF powder, and **(b)-(d)** BIF powder ball milled for 1h, 2h, and 3 h respectively. The gravity center (GC), the derived interlayer distance, and the area under each curve are indicated.

Table 3-4 Deconvolution data of the asymmetric XRD peak found in the range of 24-28 degrees. Three curves were used. The gravity center refers to angle value (2θ) where the curve exhibited the maximal height (intensity). The deconvoluted peak can be seen in Figure 3-23.

Sample	Peak Type	Gravity Center	Max. Height	FWHM	Area Fit
0 h	Gaussian	25.72	214.05	1.0309	17.41
	Gaussian	26.47	878.80	0.8005	55.51
	PsdVoigt1	26.74	1239.90	0.2154	27.07
1 h	Gaussian	25.93	163.20	1.33	29.33
	Gaussian	26.37	424.71	0.66	38.21
	PsdVoigt1	26.70	821.09	0.20	32.45
2 h	Gaussian	26.06	394.79	1.24	29.27
	Lorentz	26.42	1003.71	0.66	52.28
	Lorentz	26.74	675.79	0.33	18.43
3 h	Gaussian	26.08	342.96	1.28	27.75
	Lorentz	26.39	826.64	0.68	46.83
	Lorentz	26.73	777.96	0.37	25.41

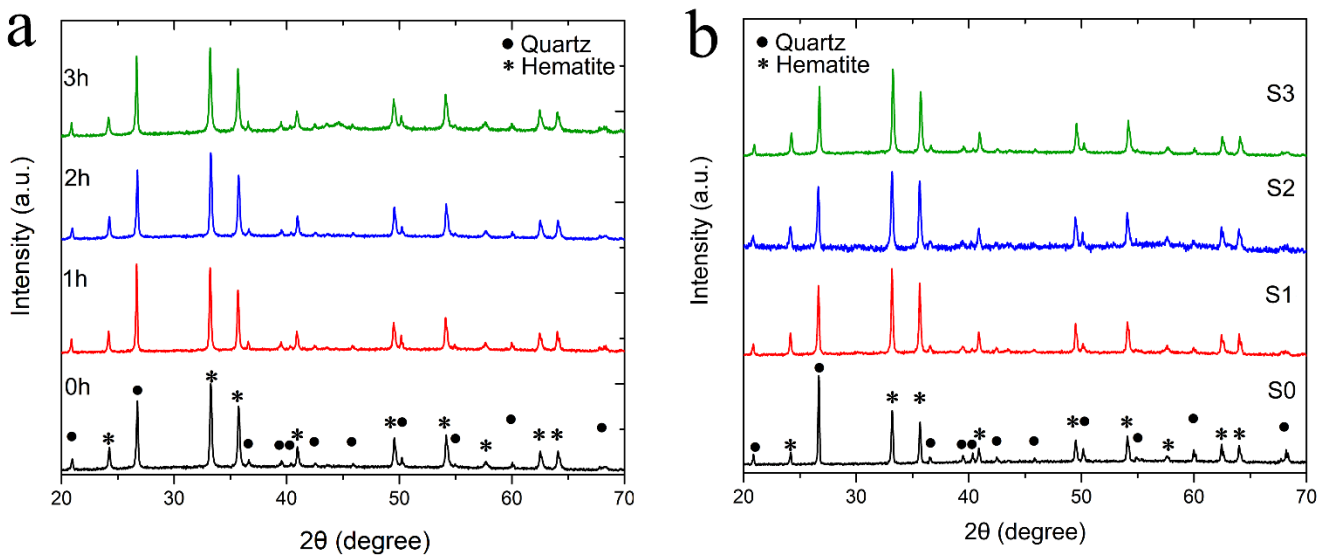

Figure 3-24 XRD patterns of remaining materials in the TGA measurements (collected residuals after the TGA measurement). **(a)** Results for BIF powders, as received ball milled during 1, 2, and 3 h, **(b)** Results for N-MWCNT samples (S0, S1, S2, and S3) grown on BIF powders. In all cases, the quartz and hematite structures were obtained.

3.5 X-ray Photoelectron Spectrometry

To understand the surface chemistry of the synthesized carbon nanomaterials XPS characterizations were performed for each sample. Figure 3-25 show the four XPS surveys corresponding to S0, S1, S2 and S3 samples. In all cases it was possible to detect carbon, oxygen, nitrogen elements. Si was not detected in survey of sample S2, which is the sample that did not present residual in the TGA results. In the case of S1, it was possible to detect two peaks corresponding to kind of Si bonds, namely Si2p and Si2s, which means that in the fabrication of this sample, all the SiO_2 present in the powder was not utilized during the AACVD process.

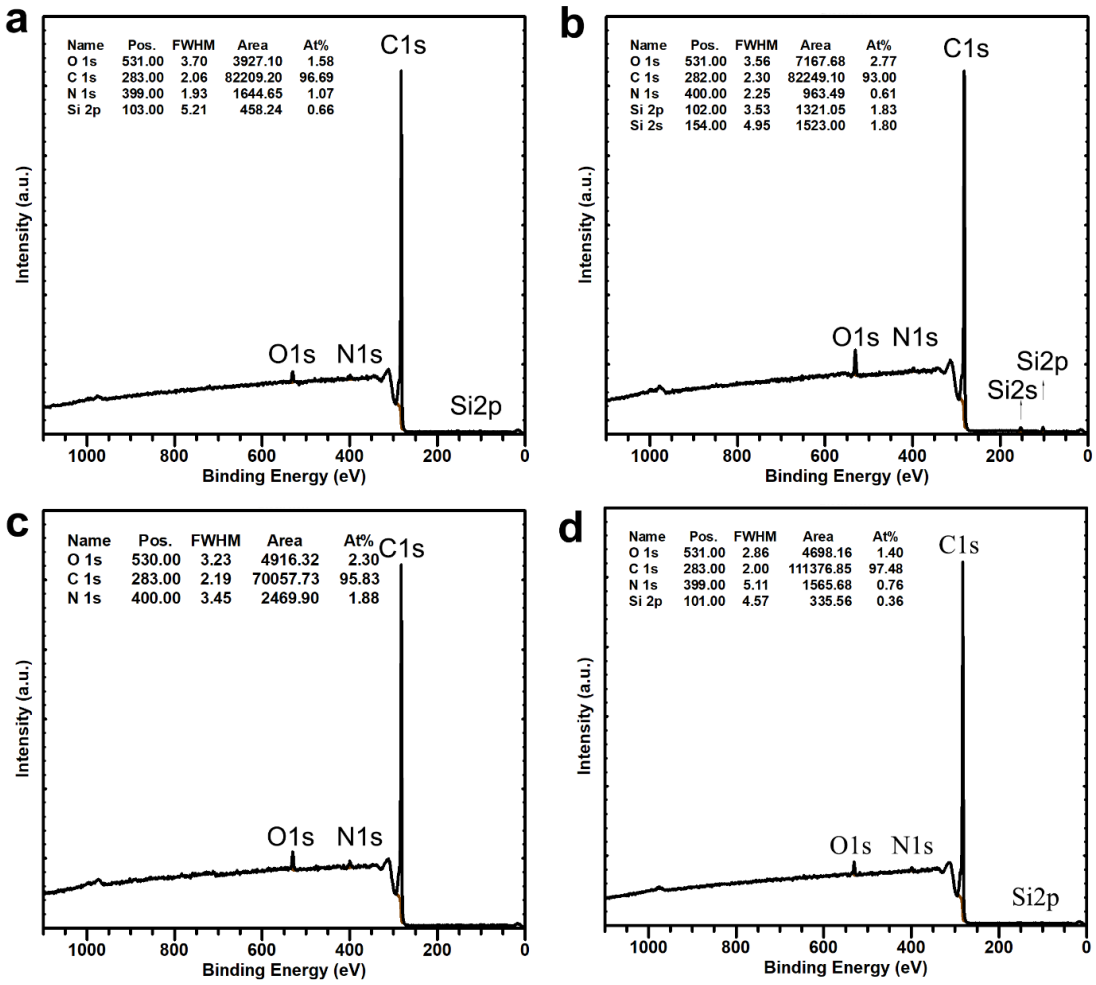

Figure 3-25 XPS survey spectrum of **(a)** N-MWCNTs grown on as received BIF powder S0, and N-MWCNTs grown over milled BIF powders for 1,2 and 3 hours, S1-S3 **(b-d)** respectively.

Also, the residual material was around 18% of its initial weight. In general, the samples contain from 1 at% to 3 at% of oxygen, being S1 which present the highest oxygen content (2.8 at%). Carbon element is between 93 at% to 98 at%. S1 exhibit the lowest content of carbon (93.1 at. %). In the case of nitrogen content, in all of the cases is below 2 at%. The deconvoluted high resolution XPS (HR-XPS) spectra of carbon, oxygen and silica are showed in Figure 3-26 . Each row corresponds to each of the cases, beginning with case S0.

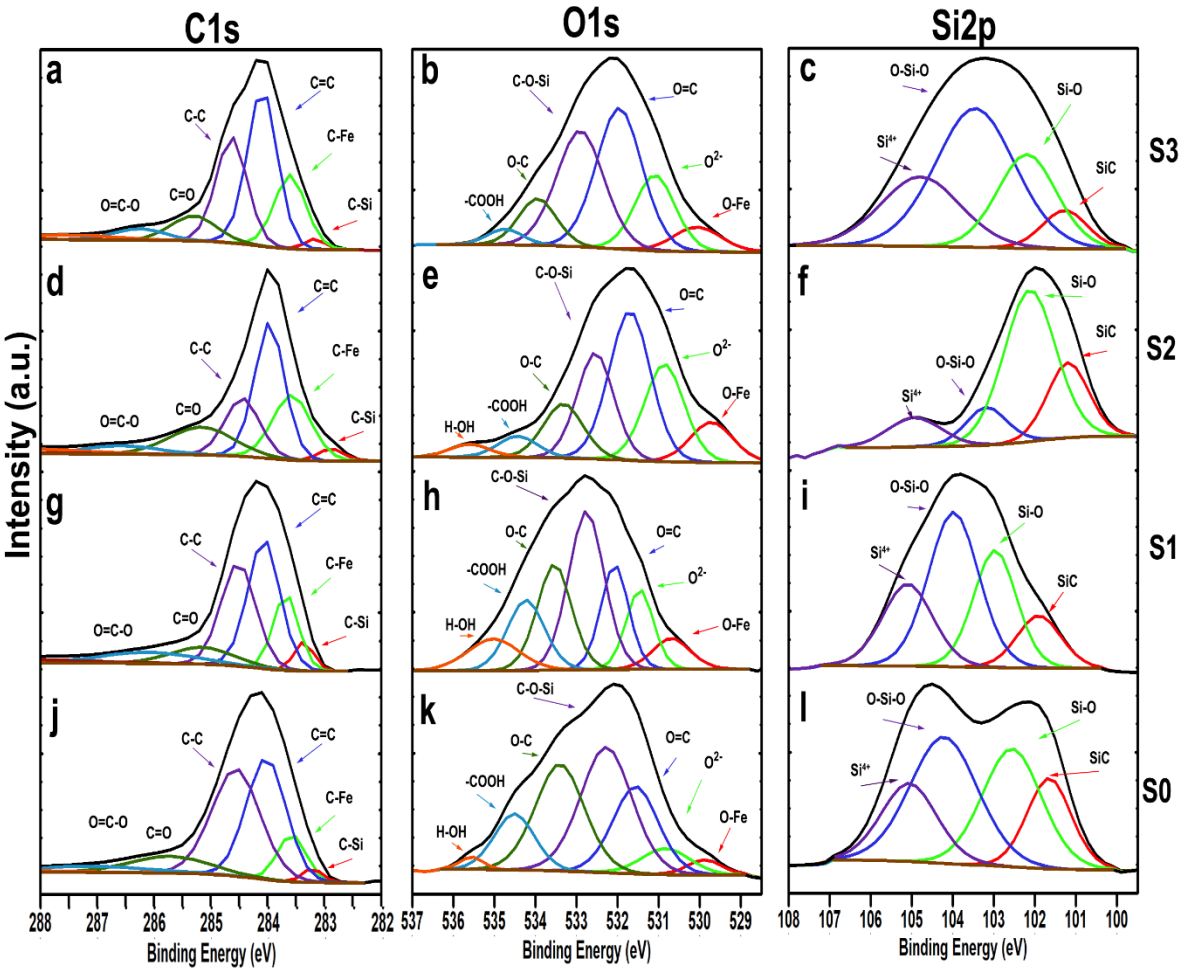

Figure 3-26 Deconvoluted high resolution XPS spectra for the synthesized N-MWCNTs. **(a)-(c)** sample S3, **(d)-(f)** sample S2, **(g)-(i)** sample S1, and **(j)-(l)** sample S0. C1s spectra (first column) showing the presence sp^2 hybridized carbons (C=C bonds), sp^3 hybridized carbons (C-C bond), and presence of carbonyl C=O and metal carbide compounds can be identified. O1s spectra (second column) showing the presence of C=O and C-O bonds. Si2p spectra (third column) reveals the presence of SiC, SiO_2, and Si-O-Si. Details on the deconvolution analysis (peak gravity center, FWHM, and percentage of the different chemical functional groups) can be seen in table 3-4 to 3-7.

The Table 3-5 to 3-7 shows the results that are showed in Figure 3-26. The peaks associated to different elements were deconvoluted, the binding energies, type of bond, FWHM, and integrated area are depicted.

In general, XPS characterizations demonstrated that the surface chemistry of the carbon nanotubes exhibited significantly differences depending on what type of BIF powder was used to its synthesis.

3.5.1 Carbon chemical composition

Basically, in the case of carbon for the four cases studied the deconvoluted carbon bonds are practically the same. C-Si (283.35 eV), C-Fe (283.67 eV), C=C (284.06), C-C (284.61 eV), C=O (285.15 eV), C=O-C (286.12 eV) and π-π (290.17 eV), bonds are present in almost all the cases. For example, C-Fe bond was not detected in the case of S2, which it was already seen that the residual was essentially absent (Figure 3-30a). The differences reside in the amount of kind of bonds that each material presents. For instance, samples S0, S1 and S3 exhibit the least amount of sp^3 C-C bonds that could be related with the fact observed in Figure 3-5, where a relatively small amount of amorphous-like carbon is present on the surface of such sample. This situation is not distinguished in S2 sample where according HR-XPS results a big amount of this bond is detected in the surface. This result could be associated with the evidence presented in TGA results where this sample exhibited a larger amount of amorphous-like or functional groups attached to their surface (Figure 3-30a). The values of the binding energies can be seen in Table 3-5. The bond C-Si in S1 is 2.52% of C1s being the highest if we compare with the other cases. Practically, the C-Fe bond is almost the same for the most of the N-MWCNTs considered. This result could mean that iron carbide probably is the responsible for the catalyst of N-MWCNTs mainly.

Table 3-5 Deconvolution data for the expanded C1s peak, showing the binding energies, type of bonds or chemical groups, full width at half maximum (FWHM), and the integrated area. Results for as received powder (0 h) and for BIF powders ball milled for 1h, 2h, and 3h.

Sample	BE (eV)	Bond	FWHM	Area %
0 h	283.21	C-Si	0.41	1.87
	283.57	C-Fe	0.60	9.18
	284.02	C=C	0.82	32.61
	284.55	C-C	0.99	35.23
	285.71	C=O	1.63	8.93
	287.07	C=O-C	2.47	4.73
	290.32	π-π*	3.26	7.45
1 h	283.35	C-Si	0.40	4.04
	283.67	C-Fe	0.52	13.62
	284.06	C=C	0.66	29.60
	284.51	C-C	0.71	25.42
	285.15	C=O	1.32	7.71
	286.12	C=O-C	1.94	7.62
	290.17	π-π*	4.41	11.07
2 h	282.88	C-Si	0.52	2.52
	283.57	C-Fe	0.79	19.75
	283.96	C=C	0.62	32.35
	284.44	C-C	0.72	16.16
	285.16	C=O	1.33	14.29
	286.56	C=O-C	1.54	5.04
	290.6	π-π*	4.04	5.41
3 h	283.17	C-Si	0.41	1.64
	283.60	C-Fe	0.65	17.46
	284.09	C=C	0.62	35.46
	284.63	C-C	0.64	24.55
	285.30	C=O	0.93	8.46
	286.25	C=O-C	1.03	4.26
	290.38	π-π*	2.74	4.91

3.5.2 Oxygen chemical composition

For oxygen HR-XPS, -COOH (534.5 eV), O-C (533.4 eV), C-O-Si (532.2 eV), O=C (531.5 eV) and Si-Fe oxides (529 eV) were well deconvoluted (Figure 3-26b and Table 3-6).

It is well known that the functional groups -COOH, and -OH are formed due to the ethanol participation in the synthesis [59]. O-Fe bond is because some Fe-oxides survived after the synthesis. However, these Fe-oxides did not were observed in X-ray characterization. Then, probably their participation in the samples is minimum. Except in the S3 case, the

participation of O^{2+} is important in O1s element. These could be associated to hydroxyl groups and nitrogenated functionalities due to the wrinkled surface of N-MWNTs, where the folds trap oxygen species. The C-O-Si is a bond that is related to the silicon carbide oxides. They were also not observed in X-rays. It is very likely that the size of these materials is very small, of very few nanometers, which is impossible to detect in XRD patterns. Functional groups H-OH, -COOH and O-C appeared as results of ethanol incorporation in the precursor solution. They are associated to the hydro response of samples. O-OH bond is not detected in S3 sample where the N-MWCNTs present a large diameter distribution from few to hundred nm, being to the most notorious the fibrous carbon nanotubes (see Figure 3-5d). In the other cases this bond is relatively small (1.4 %) (S0) that could imply less hygroscopic behavior.

Table 3-6 Deconvolution data for the expanded O1s peak, showing the binding energies, type of bonds or chemical groups, full width at half maximum (FWHM), and the integrated area. Results for as received powder (0 h) and for BIF powders ball milled for 1h, 2h, and 3h.

Sample	BE (eV)	Bond	FWHM	Area %
0 h	529.88	O-Fe	0.99	2.55
	530.82	O^{2-}	1.37	6.30
	531.56	O=C	1.30	19.83
	532.27	C-O-Si	1.47	32.35
	533.40	O-C	1.40	26.23
	534.51	-COOH	1.15	11.30
	535.55	H-OH	0.66	1.44
1 h	530.69	O-Fe	1.08	5.87
	531.46	O^{2-}	0.78	11.01
	532.07	O=C	0.79	14.68
	532.76	C-O-Si	1.02	26.83
	533.54	O-C	0.98	18.36
	534.23	-COOH	1.06	13.22
	535.02	H-OH	1.47	8.22
2 h	529.71	O-Fe	1.23	9.00
	530.86	O^{2-}	1.14	20.25
	531.70	O=C	1.18	32.07
	532.54	C-O-Si	1.05	20.25
	533.32	O-C	1.14	11.25
	534.43	-COOH	1.15	4.44
	535.60	H-OH	1.15	2.73
3 h	530.06	O-Fe	1.36	6.34
	531.09	O^{2-}	1.15	16.48

	531.96	O=C	1.31	34.86
	532.91	C-O-Si	1.36	29.79
	533.95	O-C	1.08	9.51
	534.74	-COOH	1.03	3.02

3.5.3 Silicon chemical composition

The high resolution of Si2p for each S0-S3 sample is different. For example, S0 sample, present a homogeneous participation of Si4+, O-Si-O, Si-O and SiC bonds (Figure 3-26l). Its high resolution Si2p spectrum is two peaks curve, where O-Si-O and Si-O are the responsible of such structure. This means that the oxides did not were completely used in the CNT synthesis. Probably, because of their high size of as produced BIF particles they were not sufficiently reduced and the iron was not completely employed to the growing of carbon nanomaterial. N-MWCNTs obtained from 1h ball milled BIF present a very different high resolution XPS of Si2p (Figure 3-26i). Although the percentages of SiC, Si-O, O-Si-O and Si^{4+} are apparently the same, there is no two peak curves anymore. Nevertheless, S0 present only one third of Si2p bonds than the amount present in S1 sample (Figure 3-25b). The HR-XPS of Si2p for the N-MWCNT 2h case is particularly interesting. In this atypical sample the Si-O is the main bond compared with the SiC or O-Si-O bond. Also, the Si4+ bond is reduced being only the 11.07 wt.% of the total. SiO_x represents the bond between an atom of Si with O_2. The broad HR-XPS curve corresponding to de 3h case is built of similar form than the case 1h, the difference between these two cases is that in the case of 3h the curve representing O-Si-O is more intense, that means that after 2 hours of ball milling is possible the formation of SiO_2 structures which could be increased the weight of sample.

Table 3-7 Deconvolution data for the expanded Si2p peak, showing the binding energies, type of bonds or chemical groups, full width at half maximum (FWHM), and the integrated area. Results for as received powder (0 h) and for BIF powders ball milled for 1h, 2h, and 3h.

Sample	BE (eV)	Bond	FWHM	Area %
0 h	101.65	Si-C	1.27	16.74
	102.55	Si-O	1.69	29.21
	104.21	Si-O-Si	1.94	35.86
	105.06	Si4+	1.59	18.19
1 h	101.90	Si-C	1.25	11.90
	102.97	Si-O	1.23	26.19
	103.98	O-Si-O	1.44	40.48
	105.10	Si4+	1.44	21.43
2 h	101.19	Si-C	1.19	22.13
	102.12	Si-O	1.49	55.73
	103.18	O-Si-O	1.19	11.07
	104.93	Si4+	1.53	11.07
3 h	101.26	Si-C	1.29	7.3
	102.19	Si-O	1.70	23.36
	103.45	O-Si-O	2.27	46.21
	104.78	Si4+	2.27	23.11

3.5.4 Nitrogen chemical composition

In Figure 3-27 the 4 HR-XPS spectra for N1s of all samples is exhibited. N_2/C, graphitic-N, pyrrolic-N, pyridinic-N, and SiN could be deconvoluted from each sample. The S0 case presented an additional band representing probably the nitrogen pyridinic oxide bond. In Figure 3-27a correspond to N-MWCNT fabricated utilizing as received BIF powder and (c) to (d) are N-MWCNTs fabricated using BIF powders ball milled for 1h, 2h, and 3 h respectively. Quantitative details on the deconvolution analysis (peak gravity center, FWHM, and percentage of the different chemical functional groups) can be seen in table SI-8. The total nitrogen concentration is 1.07 at%, 0.61 at%, 1.88 at%., and 0.76 at% for 0h, 1h, 2h and 3h samples, respectively. The samples content in all cases is lesser than the N-MWCNT fabricated with conventional mixed solution of benzylamine an ferrocene which is around 2.0 % [60]. Probably, the combination of Si and oxygen passivate the nitrogen inclusion in the graphitic network. However, this interaction is crucial in the yield of carbon nanotubes. For example, when toluene was used as precursor, the production of carbon nanotubes obtained was of ~2,570 wt.% of the catalyst weight.

In general, XPS characterizations demonstrated that the surface chemistry of the carbon nanotubes exhibited significantly differences depending on the time of ball milling used to prepare the BIF powder used in its synthesis. It seems that the 2h of ball milling is crucial for obtaining a large yield of N-MWCNT with high quality. For instance, notice in Figure 3-26f how 2 h of ball milling dramatically change the functionalities of silicon. These changes are determinant in the production of N-MWCNTs. In this case most of the bonds in the sample are of Si-O type diminishing the O-Si-O type.

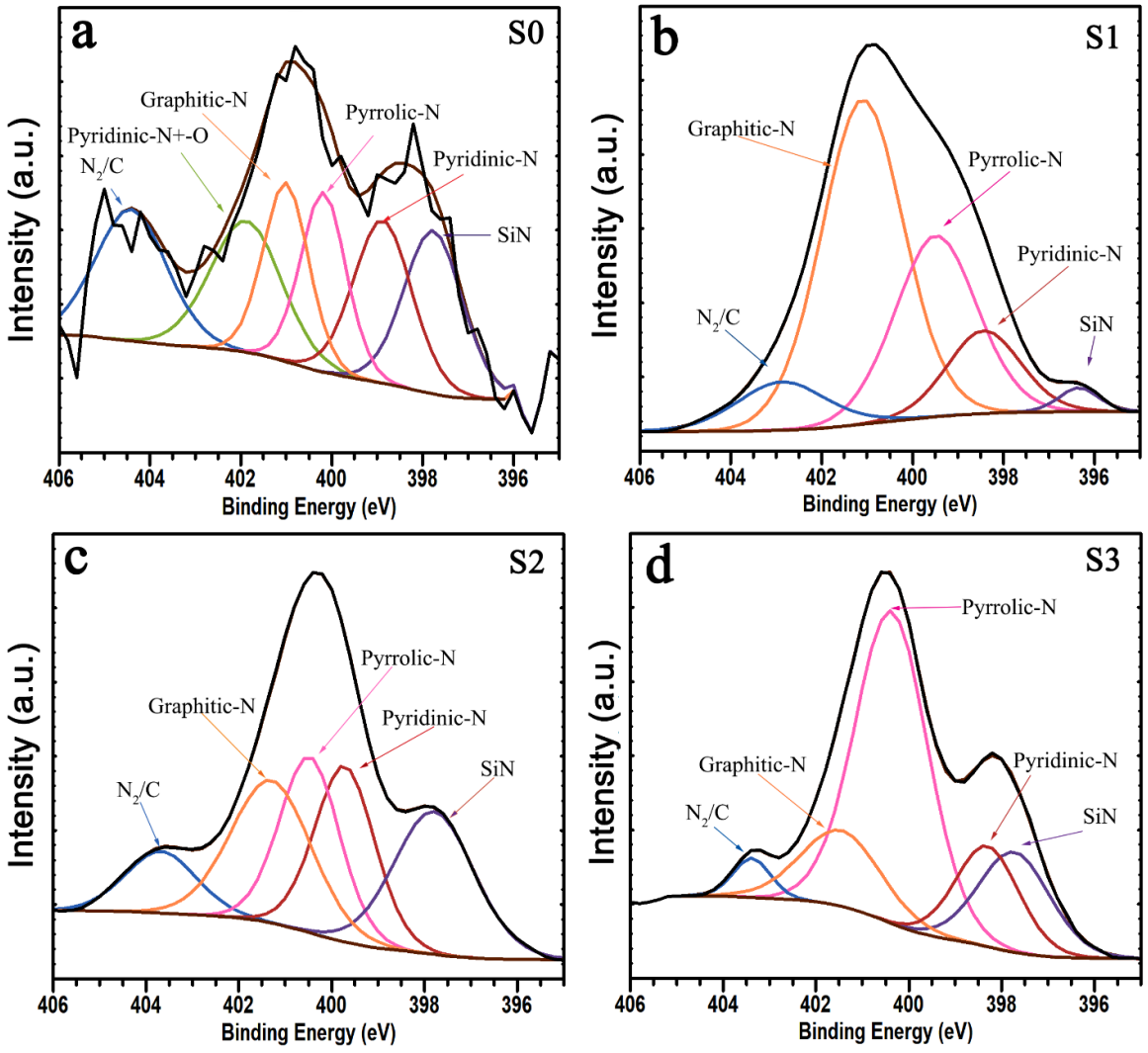

Figure 3-27 Deconvoluted high-resolution N1s XPS spectra for N-MWCNTs samples (S0, S1, S2, and S3). Presence of SiN, pyridinic-N, pyrrolic-N, graphitic-N and molecular nitrogen adsorbed on C surface can be identified. Details on the deconvolution analysis (peak gravity center, FWHM, and percentage of the different chemical functional groups) can be seen in tables 3-7.

Table 3-8 Deconvolution data for the expanded N1s spectrum, showing the binding energies, type of bonds or chemical groups, full width at half maximum (FWHM), and the integrated area. Results for as received powder (0 h) and for BIF powders ball milled for 1h, 2h, and 3h

Sample	BE (eV)	Bond	FWHM	Area %
0 h	397.77	SiN	1.51	17.64
	398.87	Pyridinic-N	1.51	17.64
	400.18	Pyrrolic-N	1.17	15.07
	401.00	Graphitic-N	1.17	15.07
	401.87	X-N Pyridine Oxide	1.83	17.29
	404.4	N_2/C	1.83	17.29
1 h	396.34	SiN	1.03	1.82
	398.43	Pyridinic-N	1.89	11.53
	399.48	Pyrrolic-N	2.11	28.00
	401.10	Graphitic-N	2.12	50.48
	402.87	N_2/C	2.31	8.16
2 h	397.79	SiN	2.03	23.66
	399.71	Pyridinic-N	1.70	21.82
	400.67	Pyrrolic-N	1.52	21.82
	401.30	Graphitic-N	2.03	23.66
	403.67	N_2/C	1.80	9.03
3 h	397.72	SiN	1.80	16.14
	398.30	Pyridinic-N	1.72	14.61
	400.36	Pyrrolic-N	1.83	51.81
	401.45	Graphitic-N	2.03	13.94
	403.38	N2/C	0.93	3.31

3.6 Raman Spectroscopy

Raman characterizations results for N-MWCNTs are shown in Figure 3-28. The D-band, G-band, 2D-bands, D+G bands and 2D' peaks were observed. The D-band peak ~1350 cm^{-1} is related to defects in sp^2 carbons (vacancies, non-hexagonal carbon rings, edges) and G-band peak ~1590 cm^{-1} which provide information on the degree of graphitization, and 2D-band peak ~2700 cm^{-1} is related to the type of stacking (random stacking and AB stacking) and the number of graphite layers. The vertical lines refer to typical values obtained for graphite materials [36]. Figure 3-28b depicts the D-band and G-band Raman shift. Samples S1 and S2 showed a G-band Raman shift closed of that obtained for high

oriented pyrolytic graphite. Sample S1 showed the lower value of the D-band Raman shift suggesting the presence topological defects into the graphite layers. Figure 3-28c depicts the ratio between the intensities of D- and G-band peaks (I_D/I_G), also for 2D- and G-band peaks (I_{2D}/I_G). I_D/I_G estimates the graphite order, for instance, low values of I_D/I_G means a high crystallinity while high values of I_D/I_G indicate the presence of defected graphite layers. Ferrari et al (2000) investigated the I_D/I_G relation for carbon materials, by using I_D/I_G relation, they classified amorphous (a-C) and tetrahedral amorphous carbon (ta-C) [37]. Notice that N-MWCNTs of sample S3 shows a vibration mode ~1100 cm^{-1} which is related to sp^3 amorphous carbons [38], also the position of the G band in S0 and S3 moves for lower values, that is promoted by a high influence on the in-plane bond stretching vibration of C-C sp^2 due amorphous carbon [37] (Figure 3-28b).

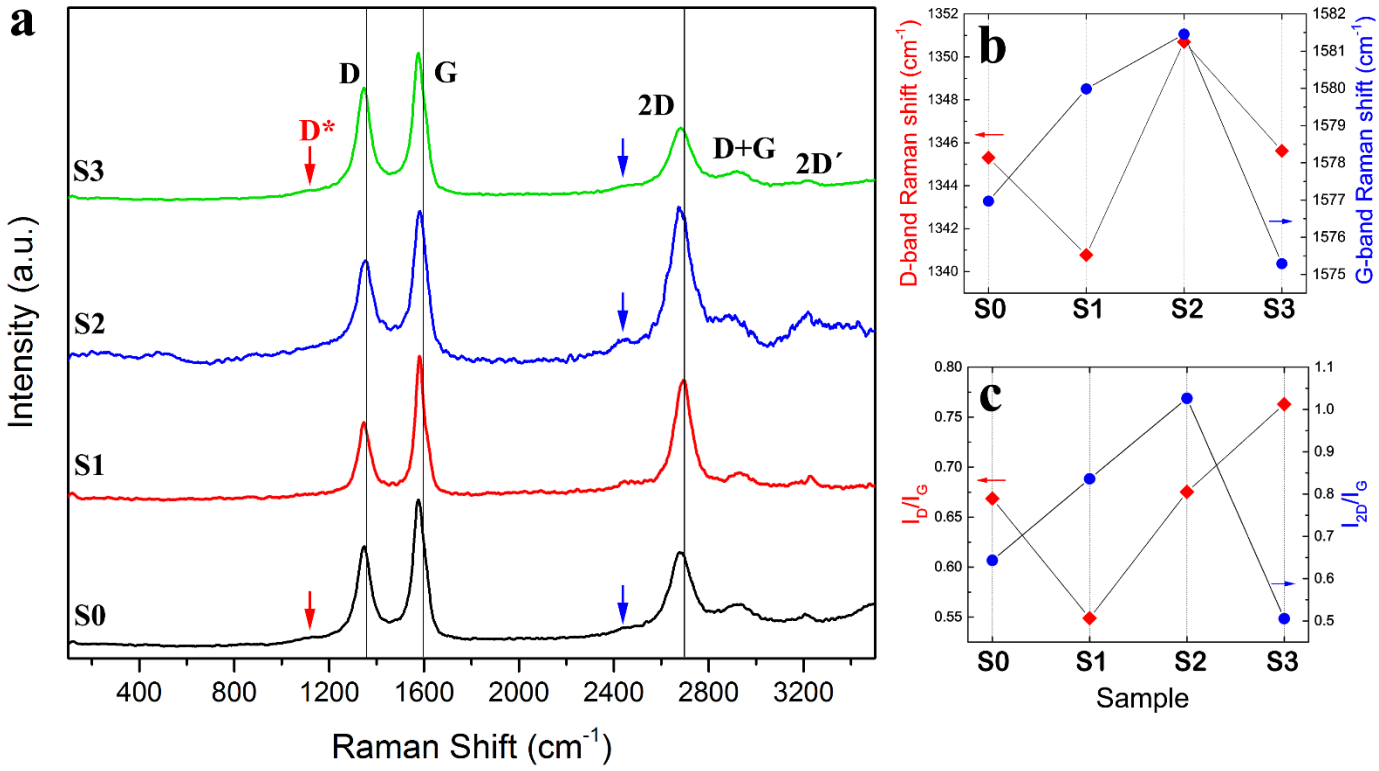

Figure 3-28 (a) Raman spectra for N-MWCNTs grown on BIF powders. Results for as received BIF powder S0 and ball milled for 1h (S1), 2h (S2), and 3h (S3), respectively. The excitation source was of 532 nm (2.33 eV) laser. The vertical lines indicate the typical values of D, G, and 2D Raman peaks in graphite. **(b)** D-band and G-band Raman shift. **(c)** The ratio of the intensity of I_D/I_G and I_{2D}/I_G. Low values of I_D/I_G indicate an improvement in the graphitization of the sample. The large intensity of 2D peak is related to few layered graphite materials.

The relation I_D/I_G for S1 and S2 samples described the formation of high crystalline carbon nanostructures as can be seen in SEM images (Figure 3-5b,c) in a contrary way, samples S0 and S3 represent more defective carbon nanostructures as the relations I_D/I_G are closer to the unity (Figure 3-28c). A vibration mode at ~2,450 cm^{-1} (blue arrow) are attributed to a vibration mode of few layered corrugated graphite [39]. It was also observed well defined 2D-band peaks. In particular, samples S1 and S2 with the highest intensities, exceeding the G-band peak intensity (sample S2)., this fact suggests the presence of few layered N-MWCNTs [36]. It is important to mention that 2D-band peak position is sensible to the electronic doping as was demonstrated by Das et al. [40]. The position of the 2D-band peak at 2679 cm^{-1} and the upshift G-band peak (1582 cm^{-1}) suggest a higher electron concentration due the nitrogen doping.

3.7 BET surface analysis

The textual characterizations of the materials were based on the corresponding N_2 equilibrium adsorption isotherms, determined at -196°C with a Quantachrome Instruments NOVA 2200e apparatus. Samples were degassed by 13 h keeping a heating temperature of 200°C then N_2 gas was used as analysis gas to be physisorbed on the carbon nanotubes surface. BET surface area (S_A) of the samples were calculated.

The Figure 3-29 illustrates the surface area isotherms for the S0-S3 samples where the behavior is characteristic of type II isotherms from weak interaction between the adsorbed gas and the MW-CNT. Sample S0 and S2 have an unusual behavior that can be compared with a straight line, due the characteristic of the isotherm, the monolayer volume is low indicative of the formation of multilayer adsorption. Sample S0 and S2 has the higher concentration of micro porosity (Figure 3-29b).

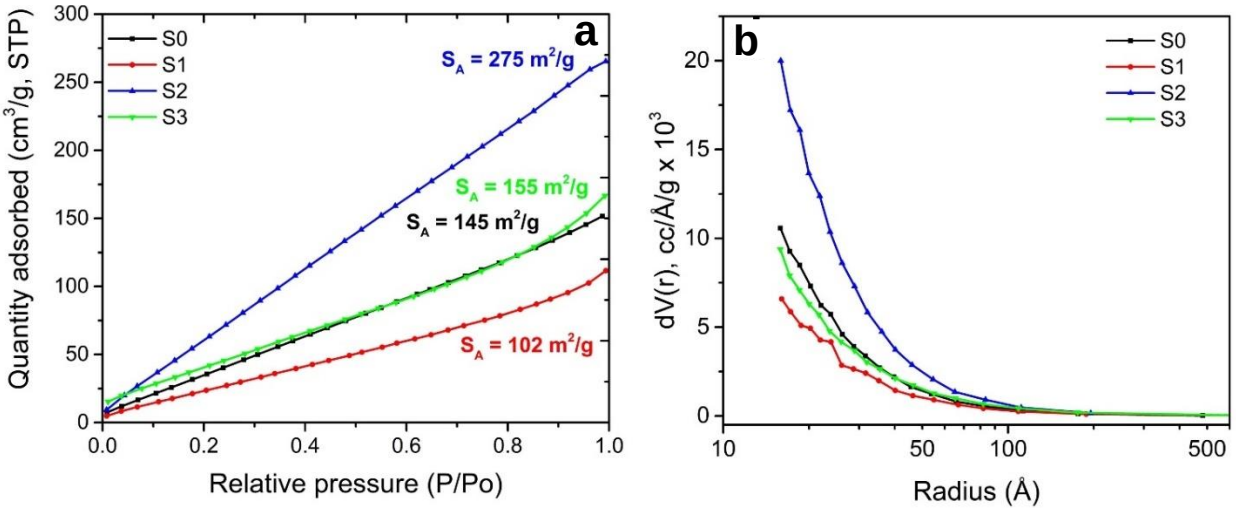

Figure 3-29 (a) N_2 physisorption isotherms type II for samples S0-S3 where S2 has the higher surface area (275 m2/g). **(b)** Pore size distribution.

Å

3.8 Thermogravimetric Analysis

TGA curves for the different N-MWCNTs revealed interesting trends (Figure 3-30). In all samples, it was observed a monotonous decrease of the weight sample as the temperature increase. The loss weight become up to 3-9 % at 500 °C. For example,

samples S0, S1 and S3 exhibited a lost weight of 4% at 500 °C whereas sample S2 lost 6% of its weight. This behavior suggests the presence of chemical functional groups attached on the carbon nanotube surface, being sample S2 the most functionalized. The oxidation temperature increased for N-MWCNTs synthesized with ball milling BIF powders (see Figure 3-30b). Notice that N-MWCNTs grown on pristine BIF powder showed the lowest oxidation temperature (522 °C)

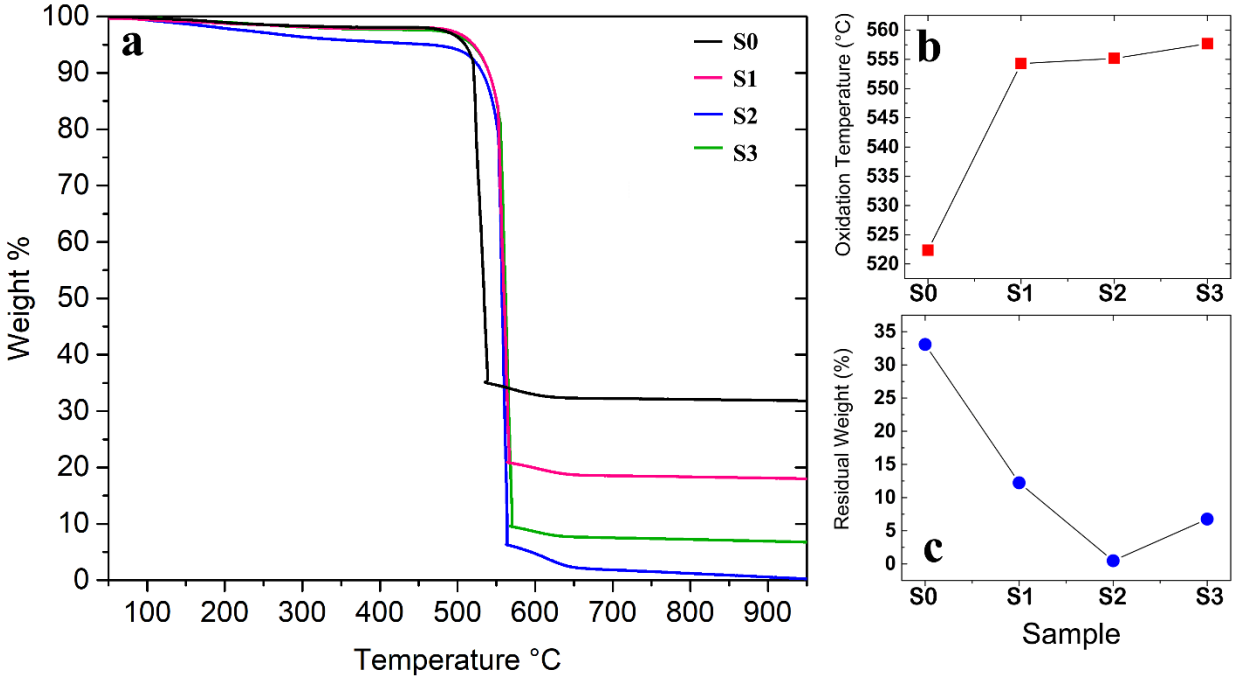

Figure 3-30 (a) TGA measurements for N-MWCNTs grown on BIF powders. Results for as received BIF powder S0 (0 h) and BIF powder subjected to a ball milling treatment for 1 h (S1), 2 h (S2), and 3 h (S3), respectively. **(b)** Oxidation temperature and **(c)** final weight (residual) obtained at 950 °C. Notice that samples S0 and S1 showed a high residual material with 32% and 18 % of the total weight, respectively.

Figure 3-30c depicts the residual material collected after finishing TGA measurement. Samples S0 exhibited the highest weight residual (33 %). This fact could be related to grain size of BIF powder, notice that sample S0 was synthesized with pristine BIF powder containing large particles. It is clear that the residual materials in the TGA experiment should be proportional to the amount of Si and Fe in the samples. Since the grain size of BIF powder decrease with the ball milling time, it is expected that small grains exhibit a higher surface/volume ratio which could favor the detached and transportation of Si and Fe to the trap in the AACVD experiment. However, other situation related to the

coalescence of particles, changes in the composition and stoichiometry with the increase of milling time should be taken account. For instance, sample S3 exhibited 5% whereas sample S2 almost null residual weight (see Figure 3-30c). The residuals are also analyzed by XRD (Figure 3-24b), showing the presence of α-SiO_2 and hematite structures.

3.9 Magnetic properties of N-MWCNTs synthesized on BIF powder substrates

Figure 3-31 shows the magnetic properties of N-MWCNTs samples. The measurements were performed at 300 K. The hysteresis loops depend strongly that how the N-MWCNTs were synthesized (Figure 3-31a), important changes in the coercive field, remanent magnetization and saturation magnetization can be identified. For instance, sample S0 produced by pristine BIF powder exhibited the highest saturation magnetization followed for samples S1, S3, and S2. The increase in saturation magnetization could be related to the size of the nanoparticles and the amount of each different phase contained in each sample. It seems that with the long time of the ball milling, the saturation magnetization decreases. This effect has been previously observed [41].

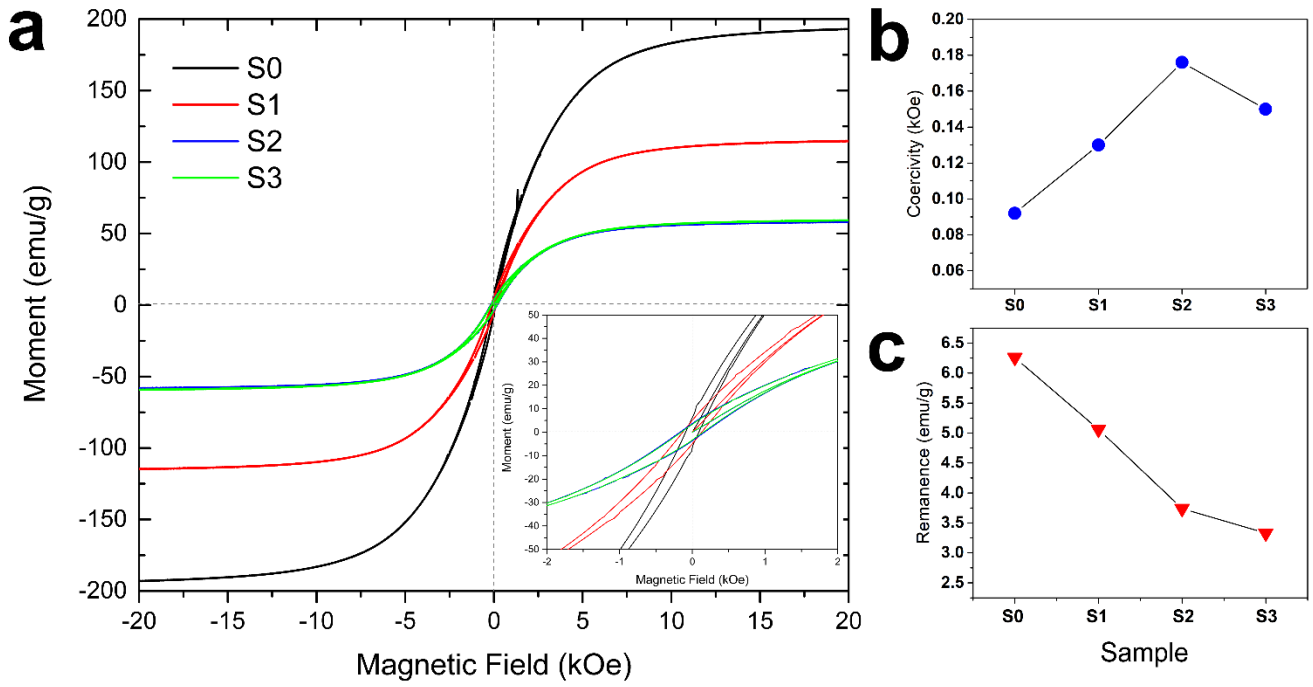

Figure 3-31 Magnetic properties of N-MWCNT samples (S0, S1, S2 and S3). **(a)** Hysteresis loops, **(b)** Coercive field, and **(c)** remanent magnetization. The inset in **(a)** shows a close up around low magnetic field

All the samples present very small coercive field (0.09-0.18 kOe). However, only the sample S0 present the same magnitude of the coercive field (left and right sides). It could be present a bias shift due to the presence of antiferromagnetic/ferromagnetic interfaces likely of core shell nanoparticles or coupled coalesced nanoparticles with different magnetic properties as another author have reported [42]. According to the X-ray diffraction, the samples contains Fe_3C and α-Fe phases, we would have expected that samples of nanotubes obtained with ball milled BIF powder (samples S1, S2, and S3) to have more iron due to the contribution of iron released from the walls of the vials in the ball milling process. We proposed a possible scenario, during the reduction process which is carried out in the reactor, 20 minutes before introducing the benzylamine vapor, the hematite structures were transformed in alpha-iron structure, here the oxygen and iron are released from the hematite structure and transported to the trap (see the AACVD experimental setup). The release of iron could be increased for ball milled BIF powder due to the grain size reduction where larger surface-volume ratio should be dominated. This fact could be confirmed by an exhaustive analysis of the chemical composition of material hosted in the trap. The coercive field shows a maximal value for samples synthesized with milled BIF powders (see Figure 3-31b). This fact could be related to the size of magnetic nanoparticles, for larger diameter of magnetic particles the coercive field should decrease [43]. In this case, the inversion of the magnetization is carried out from the multi- to the single-domain state. Notice also that samples retain a small fraction of the saturation magnetization when the external magnetic field is removed (see Figure 3-31c). A decrease of the remanent magnetization is obtained for samples synthesized with BIF powder milled during long time. For instance, the remanent magnetization for S0>S1>S2>S3.

3.10 Electrochemical analysis

Figure 3-32 illustrates the comparison of the cyclic voltammetry (CV) for the S0 to S3 sample. Figure 3-32a shows the first cycle with a potential window of -0.4 to 0.9 V at a scan rate of 10 mVs-1 for sample S0 to S3 where anodic signals are visible around -0.23V (peak-A), and 0.66 V (peak-C) for S0 and S1 can be attributed to oxidative irreversible

reactions between the electrolyte and the Si atoms and Fe atoms anchored to the MW-CNT electrode respectively and oxidative phases of amorphous carbon, Sokhanvaran et al. (2014) discussed the adsorption and oxidation of Si ions over copper electrode at a potential of -0.25V [44], Zhang, et al (2017) described the influence of Si-Fe electrode on a Li-ion adsorption indicating the evolution of crystalline Si to amorphous at 0.21 V and an effect of polarization process between Fe-Si/C electrodes at 0.32 V and 0.47 V [44]; also a pair redox of the quasi-reversible oxidation and reduction of the quinone group of the MW-CNT at 0.34 V (peak B) and 0.27 V (peak B´) is visible that could be influenced by Si-Fe particles. For the case of S2 and S3 a displacement of the par redox is visible probably due low diffusion rates between the electrolyte and the electrochemical superficial species of the MW-CNT due more defective carbon materials. After three cycles (Figure 3-32b) the sample become less capacitive as a considerably reduction of the peak-A and practically no trace of peak C, while the par redox of quinone (peak B and B') moves to higher values at ~0.5 V in a quasi-reversible system reaching the 3.2 mA. The anodic intensity is related with the quantity of Si-Fe particles contained on the MW-CNT being the most capacity the S0 sample, followed by S1, S3 and S2 respectively.

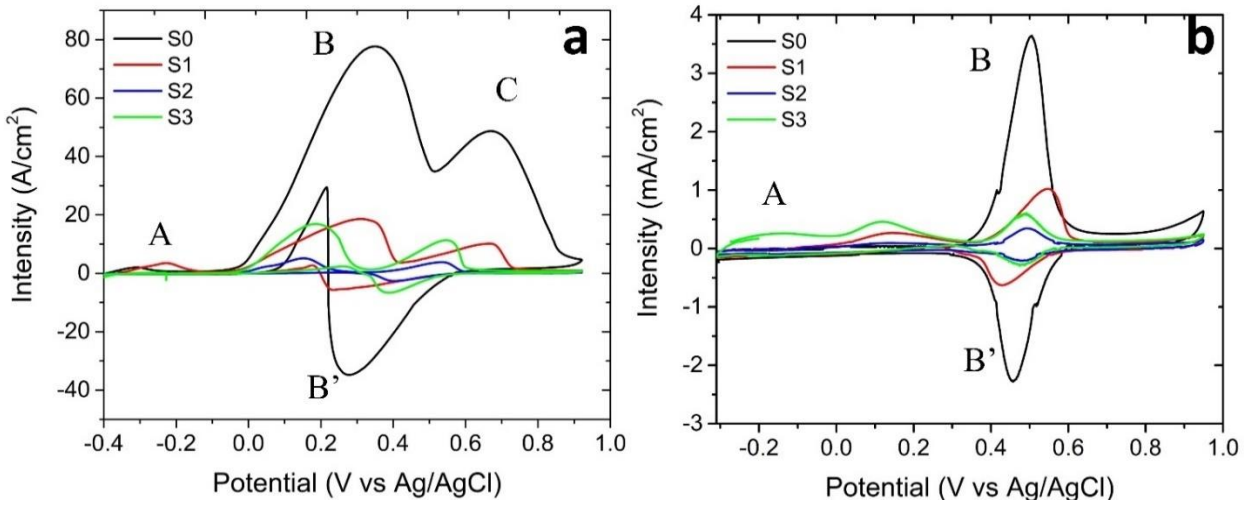

Figure 3-32 Cyclic voltammetry of N-MWCNT in a potential window between -0.4 to 0.9 V at a rate of 10 mV/s where: a) Firs cycle where three processes are visible, the A (-0.22 V) and C (0.67 V) irreversible due the phase oxidation and a reversible peak at C (0.34 V). b) After several cycle potential variations on the A and C anodic peaks are hardly visible while B peak (Quinone formation) is still observable.

3.11 Electrical properties

Figure 3-33 shows the electrical conductivity of the S0-S3 samples, measured using a 4-point probe. For the 4-point measurement, the average conductivity and standard deviation as a function of eight measurement configurations among the same sample

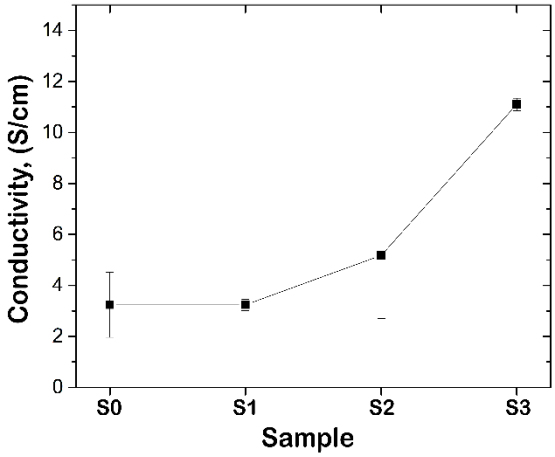

Figure 3-33 (a) Electrical conductivity of N-MWCNTs grown on as received BIF powder (S0) and ball milled for 1h, 2h, and 3h, S1-S3 respectively.

Sample S3 exhibit the highest conductivity, the increased conductivity could be associated with the pyrrolic nitrogen content within the carbon nanostructure (see Figure 3-27d) [45].

3.12 Acid and heat treatment effects on N-MWCNTs

It is well known that applications of N-MWCNTs in capacitors, supercapacitors, hydrogen storage, sensor devices, among others, a high surface area with specific chemical activity is required. In order to increase the surface area and attach different functional groups (carbonyls, carboxylics, among others), the N-MWCNTs were subjected to an acid treatment. N-MWCNTs were immersed during 30 min in an acid solution containing H_2SO_4/HNO_3 (3:1, v/v) at room temperature. N-MWCNTs synthesized on pristine BIF powder called sample S0, after acid treatment is called S0-A, similar notation is used for nanotubes synthesized on ball milling BIF powder (S1-A, S2-A, and S3-A). Firstly, we analyze the effect of the acid treatment on the structures of carbon nanotubes, Figure

3-34 displays the SEM images of N-MWCNTs after the acid treatment. We observed the removal amorphous carbon which was hosted on the surface of carbon nanotubes, also large carbon fibers were cut alongside their walls (see red arrows).

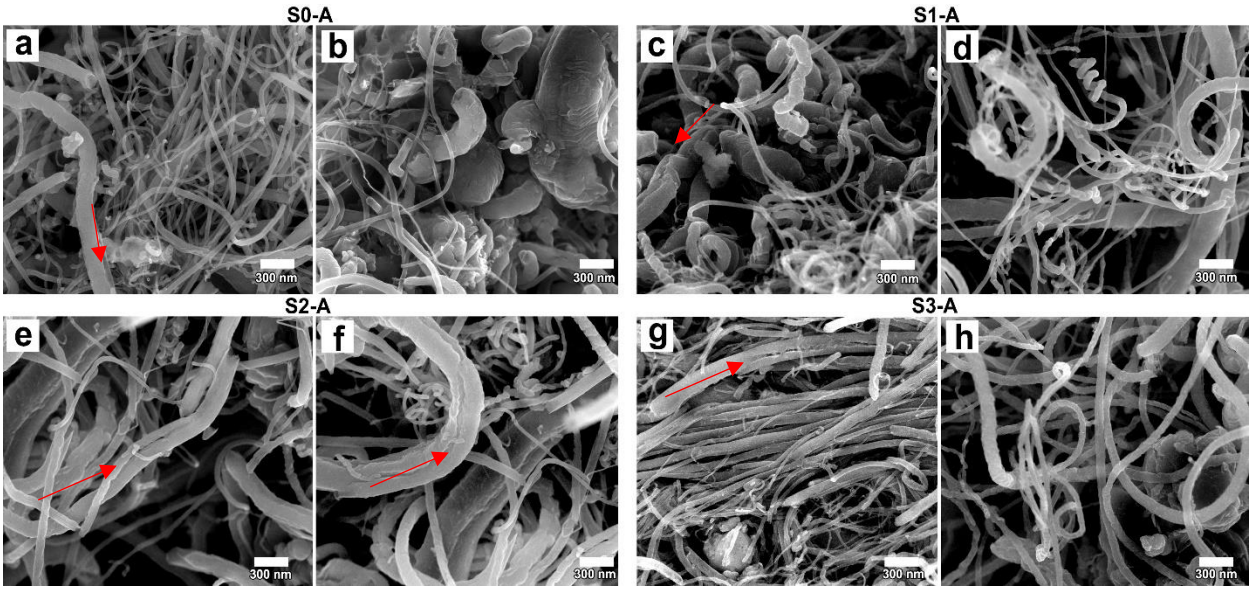

Figure 3-34 SEM images of N-MWCNTs exposed to an acid treatment for 30 min. **(a)** sample S0-A, **(b)** sample S1-A, **(c)** sample S2, and **(d)** S3-A correspond to N-MWCNTs grown on BIF powders subjected to a ball milling process during 1 h, 2h, and 3 h, respectively.

Figure 3-35 shows the TGA measurement for N-MWCNTs treated with acid, A monotonous decrease of weight samples is observed, reaching up to 10-20 % loss weight just before the oxidation temperature. In Figure 3-35b, the oxidation temperature is plotted for the four considered samples, with maximal values for samples S0-A and S3-A. When we compared the oxidation temperatures with N-MWCNTs non-treated with acid, important changes were observed for samples S0-A, S1-A, and S2-A. For instance, sample S0-A exhibits an oxidation temperature around 553 °C whereas for sample S0 it was of 522 °C. The residuals obtained after the TGA measurements (see Figure 3-35), remaining materials at 950 °C. The quantity of residuals was considerably decreased when we compared with non-acid treated carbon nanotubes due to the removal of amorphous carbon, organic materials, and metals. Therefore, it is clear that the acid treatment promotes structural and chemical activity of carbon nanotubes.

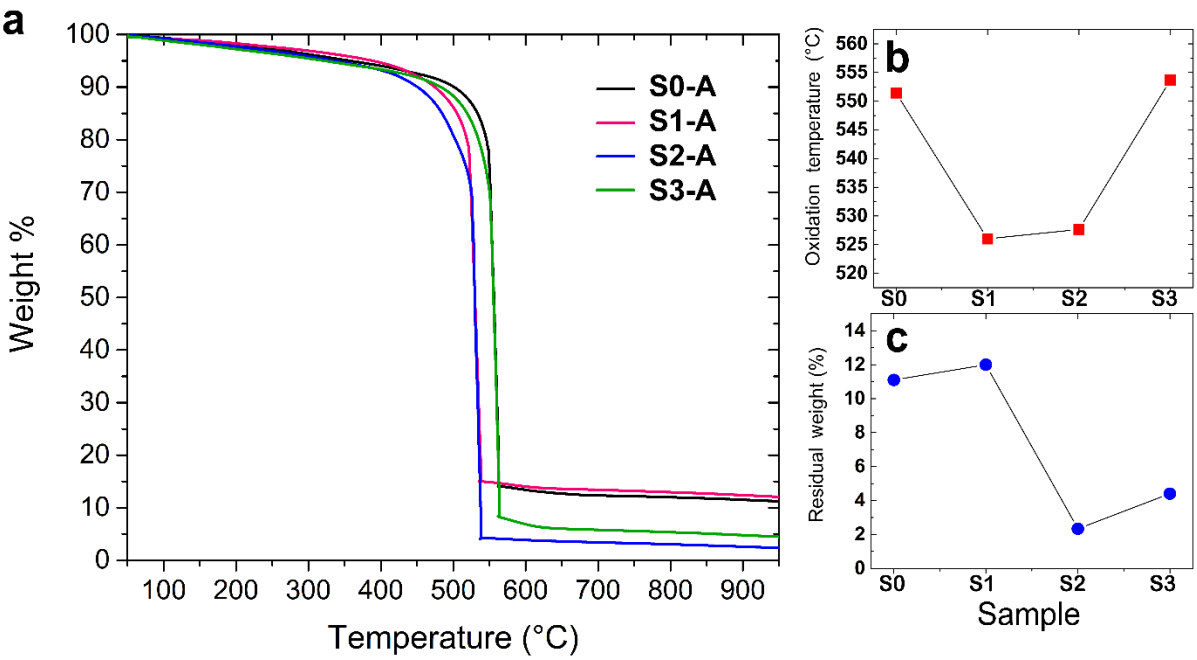

Figure 3-35 (a) TGA analysis for N-MWCNTs grown on BIF powders after acid treatment. Results for samples grown on as received BIF powder (0 h) and ball milled for 1 h, 2 h, and 3 h, respectively. Results from TGA curves: **(b)** oxidation temperature and **(c)** final weight (residual) obtained at 950 °C. Notice that the as received BIF powders and powders milled for 3 h showed almost the same oxidation temperature and samples milled for 1 and 2 h showed similar oxidation temperatures too.

N-MWCNTs samples from S1-A and S3-A materials were exposed to a heat treatment during 12 h at 430 °C in an oxidizing atmosphere. Preliminary characterizations of SEM, TEM and single point BET are shown below. Figure 3-36 displays SEM images for thermal treated samples S1-A and S3-A. Both samples exhibit small particles attached to the nanotubes surface and rough scaly morphologies are observed. However, more studies on the composition and internal structure of these particles are needed. Interestingly, SEM images of the samples thermo treated from S1-A Figure 3-36a exhibit a rugged surface that resembles a dragon skin-like morphology.

TEM images are shown in Figure 3-37 shows respective heat treated S1-A and S3-A samples, here we can observe “naked” bamboo structures” Figure 3-37b this is due the exfoliation of the graphitic surface. After the exposure of electron beam, a few amorphous materials start to grow on the surface of the CNTs Figure 3-37c, but still you can see the crystalline core layers of graphite.

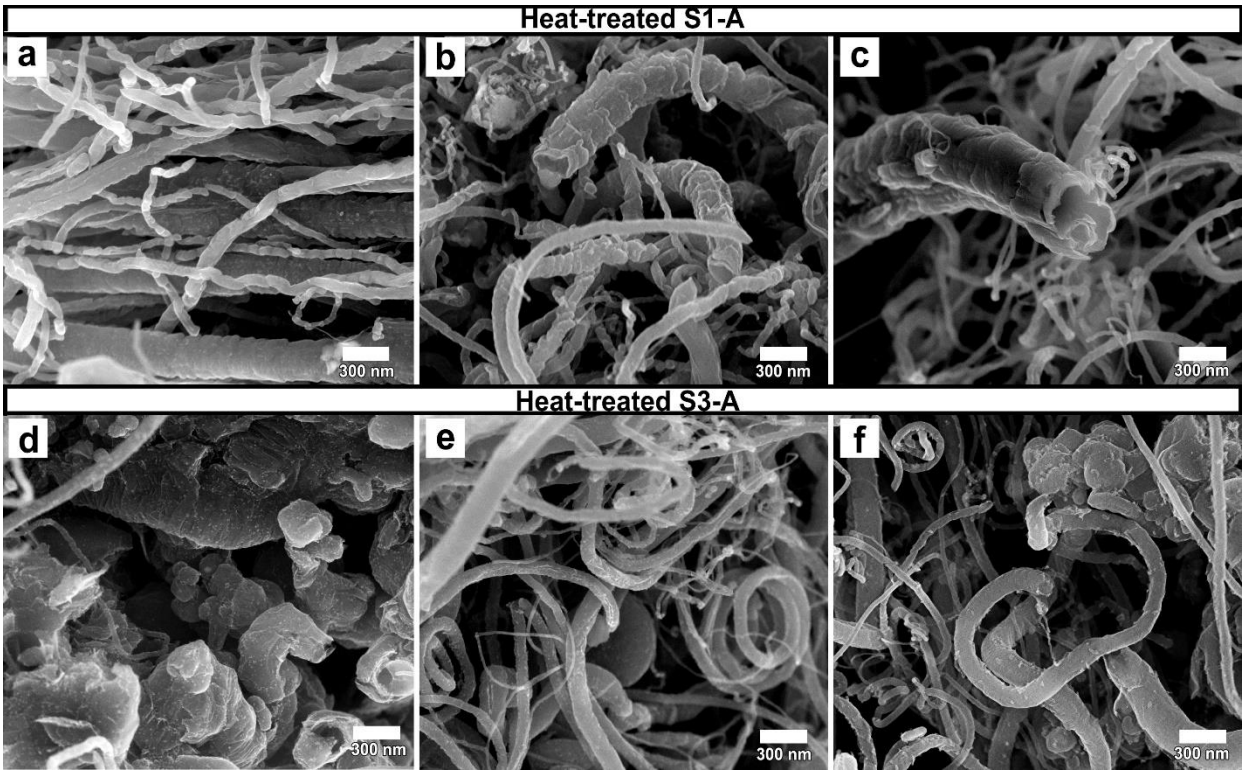

Figure 3-36 SEM images of N-MWCNTs grown on BIF powders and treated with acid during 40 min and later to a heat treatment t 430 C for 12 h. **(a-c)** Corresponds to sample S1-A and **(d-f)** to S3-A.

In Figure 3-37d-f are shown N-MWCNTs for het traded samples S3-A. It can be seen that a few crystalline particles are attached to the surface of the CNTs. However, more studies on the composition and structure of these nanoparticles are now needed. Figure 3-38 illustrate preliminary measurements of the surface area of the heat-treated samples, roughly a surface area of 1390 m^2/g is obtained for S3-A sample which is extraordinary. This may be consequence of the rugosity and complex surface seen in Figure 3-37d**.** Nevertheless, the adsorption isotherms show linearity, but yet resemble a type II curve, more studies have to be carried out to clarify this situation.

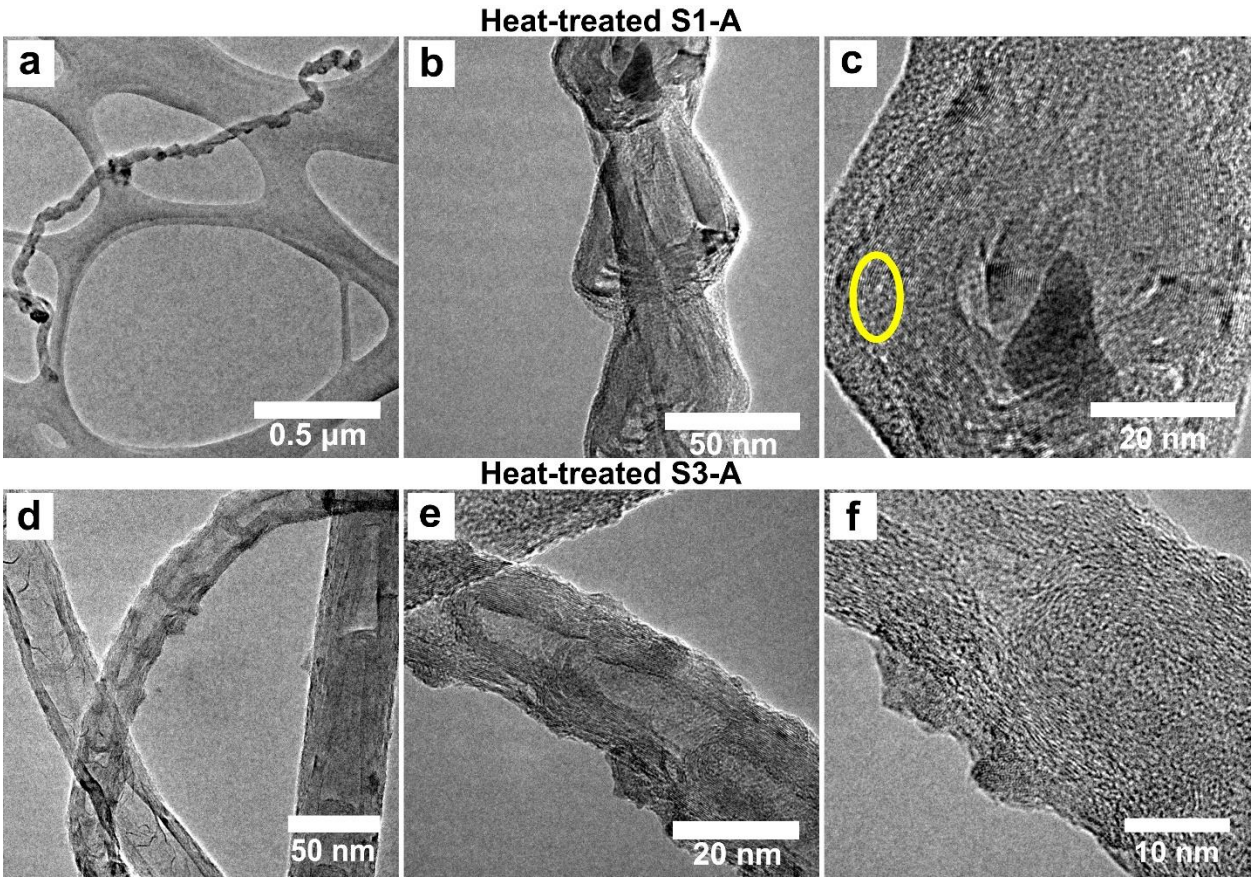

Figure 3-37 TEM images of N-MWCNTs treated with acid and exposed to a heat treatment at 430 °C for 12 h. Small nanoparticles (5-10 nm diameter) attached on the N-MWCNTs were observed for sample S3-A, as also observed in SEM image, see **Figure 3-36**d. More studies on the composition and structure of these nanoparticles are now needed.

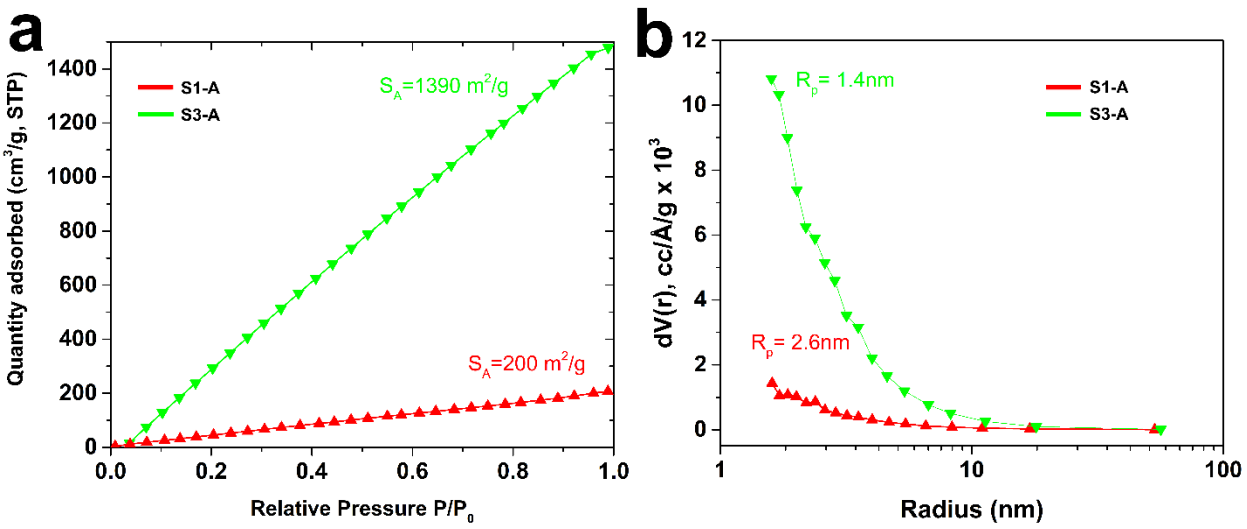

Figure 3-38 N_2 physisorption isotherms type II for heat treated samples S1A and S3-A where S3-A has the higher surface area (1390 m^2/g). (b) Pore size distribution.

Chapter 4 - Conclusions & perspectives

We demonstrated that BIF powder is an efficient catalyst for the production of N-MWCNTs Banded iron formations account for more than 60% of global iron reserves, and can be found in Australia, Brazil, Canada, India, Russia, South Africa, Ukraine, and the United States.

Pristine and ball milling BIF powders were used to produce diverse types of carbon nanotubes by means of AACVD method. Characterizations using different techniques revealed that chemical surface, morphology, diameter, electrochemical and magnetic properties of N-MWCNTs depend strongly of the used BIF powders (pristine and those ball milling treated). Yield production of up to 340 % wt./wt. showing that BIF powders could be used a massive carbon nanotube production.

Table 4-1 Production yield of conventional synthesis using ferrocene as catalyst and using BIF catalyst. Synthesis for 2.5% and 7.5% of ferrocene and BIF are calculated using grams of product between grams of catalyst per hour. (These results are for optimal conditions in an AACVD experiments)

(**2.5%** fc) 168mg → 598mg (CNx-6cm) → **Ratio 3.55 $gg^{-1}_{Cat}h^{-1}$**

(**7.5%** fc) 234mg → 844mg (CNx-6cm) → **Ratio 3.60 $gg^{-1}_{Cat}h^{-1}$**

(**BIF**) 95.9mg → 973mg (CNx-6cm) → **Ratio 10.14 $gg^{-1}_{Cat}h^{-1}$**

The synthesized samples consisted in complex N-MWCNTs branches grown in all directions with different diameters with a bamboo like structures. Brunauer–Emmett–Teller measurements revealed that N-MWCNTs exhibited high surface area of 275 m^2/g with pore radius of few nanometers (2-10nm). XPS characterizations revealed the presence of nitrogen into the graphite layers via different fashions (pyrrolic, quaternary, pyridinic, and molecular N_2) in concentrations ranged from 0.76-1.88 At%. The electrochemical response of N-MWCNTs by cyclic voltammetry exhibited well defined oxidation and reduction peaks with a large current for samples synthesized using pristine BIF powder, thus our N-MWCNTs could have used as electrodes in energy storage and sensor systems. It is important to remark that the BIF powder is a low cost material with a great potential to produce large amounts of carbon nanotubes with physico-chemical properties different of that synthesized using ferrocence and benzylamine as precursors

without a catalyst. Priliminarly, results of an acid treatment of the samples have demonstrated to increasing up to 1389 m^2/g. Also, after a heat treatment, the N-MWCNTs are decorated by small nanoparticles.

Perspectives

Additional measurements will be needed for materials with acidic and thermal treatments, including cyclic voltammetry to reveal their catalytic activity, which due to its high surface area is expected to be interesting. Subsequently, sensors with these materials will be manufactured for their gas sensing tests or biological molecules. Experimental variations will be tested, such as variation in the temperature of synthesis and different precursors and other doping agents.

The presented synthesis method of N-MWCNTs on natural mineral is also interesting from the industrial point of view, because the presented method does not need the time and cost consuming preparation of the sophisticated catalyst which are required for conventional CVD process, providing low-cost, high-quality N-MWCNTs products for developing large-scale applications in near future.

The CVD segment of the carbon nanotubes market is expected to grow at the highest CAGR during the forecast period of 2017 to 2022. The CVD method was also the largest method segment globally in 2016. This method is cheaper as compared to all others. The prices for CVD are assumed to decrease incrementally with the improving technologies and increased production & commercialization. This decrease in price is expected to keep the CAGR for CVD on a higher side for the both volume and value markets. Among type, the multi-walled carbon nanotubes segment is leading the carbon nanotubes market and is expected to grow at the highest CAGR during the forecast period. The MWCNTs find applications in electrical conductivity, conductive transparent electrodes, conductive heating films, conductive nano-inks, nano-devices, displays, chemical sensors, super batteries, supercapacitors, energy storages, solar industries, thermal interface material, and many more. The global carbon nanotubes market size is expected to reach 15.10 kilotons by 2022. In terms of value, the market size was USD 3.43 Billion in 2016, and is likely to reach USD 8.70 Billion by 2022, at a CAGR of 17.09% during 2017 to 2022.

Bibliography

[1] M. Inagaki, M. Toyoda, Y. Soneda, T. Morishita, Nitrogen-doped carbon materials, Carbon N. Y. 132 (2018) 104–140. doi:10.1016/j.carbon.2018.02.024.

[2] J.-P. Tessonnier, D.S. Su, Recent Progress on the Growth Mechanism of Carbon Nanotubes: A Review, ChemSusChem. 4 (2011) 824–847. doi:10.1002/cssc.201100175.

[3] P. En, C. Aplicadas, Nitrogen doped carbon nanomaterials for biosensing applications, (2013).

[4] C.P. Ewels, M. Glerup, Nitrogen Doping in Carbon Nanotubes, J. Nanosci. Nanotechnol. 5 (2005) 1345–1363. doi:10.1166/jnn.2005.304.

[5] Q. Wei, X. Tong, G. Zhang, J. Qiao, Q. Gong, S. Sun, Nitrogen-Doped Carbon Nanotube and Graphene Materials for Oxygen Reduction Reactions, Catalysts. 5 (2015) 1574–1602. doi:10.3390/catal5031574.

[6] P. Ayala, R. Arenal, M. Rümmeli, A. Rubio, T. Pichler, The doping of carbon nanotubes with nitrogen and their potential applications, Carbon N. Y. 48 (2010) 575–586. doi:10.1016/j.carbon.2009.10.009.

[7] K. Bazaka, M. V. Jacob, K. Ostrikov, Sustainable Life Cycles of Natural-Precursor-Derived Nanocarbons, Chem. Rev. 116 (2016) 163–214. doi:10.1021/acs.chemrev.5b00566.

[8] X. Tao, X. Zhang, J. Cheng, Y. Wang, F. Liu, Z. Luo, Synthesis of novel multi-branched carbon nanotubes with alkali-element modified Cu/MgO catalyst, Chem. Phys. Lett. 409 (2005) 89–92. doi:10.1016/j.cplett.2005.04.084.

[9] R.R. Bacsa, P. De Parseval, F. Martin, P. Serp, Geomimetic catalysis: From volcanic stones to ultra-selective Fe-Mo/Al2O3-TiO2catalysts for few-walled carbon nanotube production, Carbon N. Y. 64 (2013) 219–224. doi:10.1016/j.carbon.2013.07.054.

[10] J.P. Cheng, X.B. Zhang, Y. Ye, X.Y. Tao, F. Liu, Y. Li, G. Van Tendeloo, Natural mineral-marine manganese nodule as a novel catalyst for the synthesis of carbon nanotubes, J. Wuhan Univ. Technol. Sci. Ed. 21 (2006) 29–31. papers://d1615e34-af3c-4e3b-bbc5-9f81e658c9a8/Paper/p1313.

[11] M. Endo, K. Takeuchi, Y.A. Kim, K.C. Park, T. Ichiki, T. Hayashi, T. Fukuyo, S. Iinou, D.S. Su, M. Terrones, M.S. Dresselhaus, Simple synthesis of multiwalled carbon nanotubes from natural resources, ChemSusChem. 1 (2008) 820–822. doi:10.1002/cssc.200800150.

[12] D.S. Su, a. Rinaldi, W. Frandsen, G. Weinberg, Nanocarbons: efficient synthesis using natural lava as supported catalyst, Phys. Status Solidi. 244 (2007) 3916–3919. doi:10.1002/pssb.200776140.

[13] D.S. Su, The use of natural materials in nanocarbon synthesis, ChemSusChem. 2 (2009) 1009–1020. doi:10.1002/cssc.200900046.

[14] A. Rinaldi, J. Zhang, J. Mizera, F. Girgsdies, N. Wang, S.B.A. Hamid, R. Schlögl, D.S. Su, Facile synthesis of carbon nanotube/natural bentonite composites as a stable catalyst for styrene synthesis, Chem. Commun. (2008) 6528–6530. doi:10.1039/b815335c.

[15] S. Kawasaki, M. Shinoda, Y. Iwai, M. Ogawa, T. Hara, Y. Hattori, T. Kubota,

Mechanism of single-walled carbon nanotube growth on natural magnesite, Solid State Commun. 138 (2006) 382–385. doi:10.1016/j.ssc.2006.03.037.
[16] S. Kawasaki, M. Shinoda, T. Shimada, F. Okino, H. Touhara, Single-walled carbon nanotubes grown on natural minerals, Carbon N. Y. 44 (2006) 2139–2141. doi:10.1016/j.carbon.2006.03.015.
[17] A. Silva, M. Rosano, L. Stocker, L. Gorissen, From waste to sustainable materials management: Three case studies of the transition journey, Waste Manag. 61 (2017) 547–557. doi:10.1016/j.wasman.2016.11.038.
[18] M.-M. Titirici, R.J. White, N. Brun, V.L. Budarin, D.S. Su, F. del Monte, J.H. Clark, M.J. MacLachlan, Sustainable carbon materials, Chem. Soc. Rev. 44 (2015) 250–290. doi:10.1039/C4CS00232F.
[19] L.S. Lobo, Nucleation and growth of carbon nanotubes and nanofibers: Mechanism and catalytic geometry control, Carbon N. Y. 114 (2017) 411–417. doi:10.1016/j.carbon.2016.12.005.
[20] R. Sakthivel, K. Jayasankar, S.K. Das, B. Das, B.K. Mishra, Effect of planetary ball milling on phase transformation of a silica-rich iron ore, Powder Technol. 208 (2011) 747–751. doi:10.1016/j.powtec.2011.01.010.
[21] S.A. Shokry, A.K. El Morsi, M.S. Sabaa, R.R. Mohamed, H.E. El Sorogy, Study of the productivity of MWCNT over Fe and Fe–Co catalysts supported on SiO2, Al2O3 and MgO, Egypt. J. Pet. 23 (2014) 183–189. doi:10.1016/j.ejpe.2014.05.005.
[22] N. Katsuta, I. Shimizu, H. Helmstaedt, M. Takano, S. Kawakami, M. Kumazawa, Major element distribution in Archean banded iron formation (BIF): Influence of metamorphic differentiation, J. Metamorph. Geol. 30 (2012) 457–472. doi:10.1111/j.1525-1314.2012.00975.x.
[23] V.K. Singh, A. Slabunov, Geochemical Characteristics of Banded Iron Formation and Metavolcanics of Babina Greenstone Belt of the Bundelkhand Craton, Central India, J. Econ. Geol. Georesource Manag. 10 (2015) 63–74.
[24] V.T. Le, C.L. Ngo, Q.T. Le, T.T. Ngo, D.N. Nguyen, M.T. Vu, Surface modification and functionalization of carbon nanotube with some organic compounds, Adv. Nat. Sci. Nanosci. Nanotechnol. 4 (2013). doi:10.1088/2043-6262/4/3/035017.
[25] D.L.A. de Faria, S. Venâncio Silva, M.T. de Oliveira, Raman microspectroscopy of some iron oxides and oxyhydroxides, J. Raman Spectrosc. 28 (1997) 873–878. doi:10.1002/(SICI)1097-4555(199711)28:11<873::AID-JRS177>3.0.CO;2-B.
[26] K.J. Kingma, R.J. Hemley, Raman spectroscopic study of microcrystalline silica, Am. Mineral. 79 (1994) 269–273.
[27] I. Chourpa, L. Douziech-Eyrolles, L. Ngaboni-Okassa, J.-F. Fouquenet, S. Cohen-Jonathan, M. Soucé, H. Marchais, P. Dubois, Molecular composition of iron oxide nanoparticles, precursors for magnetic drug targeting, as characterized by confocal Raman microspectroscopy, Analyst. 130 (2005) 1395. doi:10.1039/b419004a.
[28] J.F. Fernández-Bertran, J.F. Ferná Ndez-Bertran, Mechanochemistry: an overview, Pure Appl. Chem. 71 (1999) 581–586. doi:10.1351/pac199971040581.
[29] Z. Ren, P.X. Gao, A review of helical nanostructures: Growth theories, synthesis strategies and properties, Nanoscale. 6 (2014) 9366–9400. doi:10.1039/c4nr00330f.
[30] R. Lv, L. Zou, X. Gui, F. Kang, Y. Zhu, H. Zhu, J. Wei, J. Gu, K. Wang, D. Wu,

High-yield bamboo-shaped carbon nanotubes from cresol for electrochemical application, Chem. Commun. (2008) 2046–2048. doi:10.1039/b800233a.
[31] L. Ai, J. Su, M. Wang, J. Jiang, Bamboo-structured Nitrogen-doped Carbon Nanotube Co-encapsulating Cobalt and Molybdenum Carbide Nanoparticles: An Efficient Bifunctional Electrocatalyst for Overall Water Splitting, ACS Sustain. Chem. Eng. (2018) acssuschemeng.8b01120. doi:10.1021/acssuschemeng.8b01120.
[32] Y. Yu, L. Gu, C. Wang, A. Dhanabalan, P.A. Van Aken, J. Maier, Encapsulation of Sn@carbon nanoparticles in bamboo-like hollow carbon nanofibers as an anode material in lithium-based batteries, Angew. Chemie - Int. Ed. 48 (2009) 6485–6489. doi:10.1002/anie.200901723.
[33] R. Lv, T. Cui, M.S. Jun, Q. Zhang, A. Cao, D.S. Su, Z. Zhang, S.H. Yoon, J. Miyawaki, I. Mochida, F. Kang, Open-ended, N-Doped carbon nanotube-graphene hybrid nanostructures as high-performance catalyst support, Adv. Funct. Mater. 21 (2011) 999–1006. doi:10.1002/adfm.201001602.
[34] M. Nath, B.C. Satishkumar, A. Govindaraj, C.P. Vinod, C.N.R. Rao, Production of bundles of aligned carbon and carbon-nitrogen nanotubes by the pyrolysis of precursors on silica-supported iron and cobalt catalysts, Chem. Phys. Lett. 322 (2000) 333–340. doi:10.1016/S0009-2614(00)00437-1.
[35] A.C. Ferrari, D.M. Basko, Raman spectroscopy as a versatile tool for studying the properties of graphene, Nat. Nanotechnol. 8 (2013) 235–246. doi:10.1038/nnano.2013.46.
[36] M.S. Dresselhaus, A. Jorio, M. Hofmann, G. Dresselhaus, R. Saito, Perspectives on carbon nanotubes and graphene Raman spectroscopy, Nano Lett. 10 (2010) 751–758. doi:10.1021/nl904286r.
[37] A.C. Ferrari, J. Robertson, Interpretation of Raman spectra of disordrred and amorphous carbon, Phys. Rev. B. 61 (2000) 14095. doi:10.1063/1.2219983.
[38] A. Kaniyoor, S. Ramaprabhu, A Raman spectroscopic investigation of graphite oxide derived graphene, AIP Adv. 2 (2012) 0–13. doi:10.1063/1.4756995.
[39] J.-B. Wu, M.-L. Lin, X. Cong, H.-N. Liu, P.-H. Tan, Raman spectroscopy of graphene-based materials and its applications in related devices, Chem. Soc. Rev. (2018). doi:10.1039/C6CS00915H.
[40] A. Das, S. Pisana, B. Chakraborty, S. Piscanec, S.K. Saha, U. V. Waghmare, K.S. Novoselov, H.R. Krishnamurthy, A.K. Geim, A.C. Ferrari, A.K. Sood, Monitoring dopants by Raman scattering in an electrochemically top-gated graphene transistor, Nat. Nanotechnol. 3 (2008) 210–215. doi:10.1038/nnano.2008.67.
[41] K. Tarigan, K. Y., S. D., Y.D. S., Effect of Milling times and Carbon content on Structural and Magnetic properties of Fe-Mn Alloys Effect of Milling times and Carbon content on Structural and Magnetic properties of Fe-Mn Alloys, J. Phys. Conf. Ser. 914 (2017).
[42] C. Prados, P. Crespo, J.M. González, A. Hernando, J.F. Marco, R. Gancedo, N. Grobert, M. Terrones, R.M. Walton, H.W. Kroto, Hysteresis shift in Fe-filled carbon nanotubes due to γ-Fe, Phys. Rev. B - Condens. Matter Mater. Phys. 65 (2002) 1–4. doi:10.1103/PhysRevB.65.113405.
[43] B.D. Cullity, C.D. Graham, Introduction of Magnetic Materials, Jhon Wiley & Sons, Inc, Hoboken., NJ, USA, 2009.

[44] S. Sokhanvaran, A. Danaei, M. Barati, Determination of Cell Potential for Silicon Electrodeposition, Metall. Mater. Trans. E. 1 (2014) 187–193. doi:10.1007/s40553-014-0019-4.

[45] O.Y. Podyacheva, S. V. Cherepanova, A.I. Romanenko, L.S. Kibis, D.A. Svintsitskiy, A.I. Boronin, O.A. Stonkus, A.N. Suboch, A. V. Puzynin, Z.R. Ismagilov, Nitrogen doped carbon nanotubes and nanofibers: Composition, structure, electrical conductivity and capacity properties, Carbon N. Y. 122 (2017) 475–483. doi:10.1016/j.carbon.2017.06.094.